Modal and Nonmodal Symmetric Perturbations. Part II: Nonmodal Growths Measured by Total Perturbation Energy

QIN XU

NOAA/National Severe Storms Laboratory, Norman, Oklahoma

TING LEI AND SHOUTING GAO

Institute of Atmospheric Physics, Beijing, China

(Manuscript received 26 April 2006, in final form 2 November 2006)

ABSTRACT

Maximum nonmodal growths of total perturbation energy are computed for symmetric perturbations constructed from the normal modes presented in Part I. The results show that the maximum nonmodal growths are larger than the energy growth produced by any single normal mode for a give optimization time, and this is simply because the normal modes are nonorthogonal (measured by the inner product associated with the total perturbation energy norm). It is shown that the maximum nonmodal growths are produced mainly by paired modes, and this can be explained by the fact that the streamfunction component modes are partially orthogonal between different pairs and parallel within each pair in the streamfunction subspace. When the optimization time is very short (compared with the inverse Coriolis parameter), the nonmodal growth is produced mainly by the paired fastest propagating modes. When the optimization time is not short, the maximum nonmodal growth is produced almost solely by the paired slowest propagating modes and the growth can be very large for a wide range of optimization time if the parameter point is near the boundary and outside the unstable region. If the parameter point is near the boundary but inside the unstable region, the paired slowest propagating modes can contribute significantly to the energy growth before the fastest growing mode becomes the dominant component.

The maximum nonmodal growths produced by paired modes are derived analytically. The analytical solutions compare well with the numerical results obtained in the truncated normal mode space. The analytical solutions reveal the basic mechanisms for four types of maximum nonmodal energy growths: the PP1 and PP2 nonmodal growths produced by paired propagating modes and the GD1 and GD2 nonmodal growths produced by paired growing and decaying modes. The PP1 growth is characterized by the increase of the cross-band kinetic energy that excessively offsets the decrease of the along-band kinetic and buoyancy energy. The situation is opposite for the PP2 growth. The GD1 (or GD2) growth is characterized by the reduction of the initial cross-band kinetic energy (or initial along-band kinetic and buoyancy energy) due to the inclusion of the decaying mode.

1. Introduction

It is widely recognized that the fastest growing mode alone will not necessarily account for all the structures observed in unstable flows. When the modes are not orthogonal, their certain linear combinations can yield nonmodal growths (measured by a well-defined norm) faster than any mode growths over physically relevant time scales (Farrell 1984; Buizza and Palmer 1995; Farrell and Ioannou 1996). To study nonmodal symmetric perturbations, the classic symmetric modes are expanded into a complete set in Xu (2007, hereafter Part I) and this set of normal modes can be used to construct any nonmodal solutions for symmetric perturbations governed by the model equations. As a sequel of Part I, the current study concerns how to combine the normal modes to yield the maximum nonmodal growth of total perturbation energy [see (4.4) and (6.3) of Part I] for a given optimization time and given horizontal wavenumber and basic-state Richardson number. As shown in Part I, the normal modes are nonorthogonal (measured by the full-space inner product associated with the total

Corresponding author address: Qin Xu, National Severe Storms Laboratory, 120 David L. Boren Blvd., Norman, OK 73072.
E-mail: qin.xu@noaa.gov

DOI: 10.1175/JAS3973.1

perturbation energy norm), but their streamfunction component modes are orthogonal between different pairs and initially parallel within each pair in the streamfunction subspace. Based on these properties, one may speculate that the maximum nonmodal growths of symmetric perturbations may be produced mainly by paired modes. This speculation will be verified and quantified in this paper.

The paper is organized as follows. In the next section, the problem of solving for the maximum nonmodal energy growth is formulated into an eigenvalue problem in the space spanned by a truncated set of the normal modes. The maximum nonmodal growths are computed in the truncated normal-mode space and the related nonmodal structures are examined in terms of combinations of the normal modes in section 3. The nonmodal growths produced by paired modes are solved analytically in section 4 and the analytical results are used to reveal the simplicity of the physical mechanism for the nonmodal growths computed in section 3. Based on the analytical results and their close comparisons with the numerical results, the maximum nonmodal growths are classified into four types in section 5. Conclusions follow in section 6.

2. Nonmodal solutions and singular vectors

In this section, we will formulate the eigenvalue problem that allows to compute the maximum nonmodal energy growth for any given optimization time. As explained in section 6 of Part I, the maximum nonmodal growth can be examined for each given horizontal wavenumber. In particular, as shown in (6.9) of Part I, the nonmodal solution can be constructed by

$$\mathbf{q}(x, z, t) = \sum_j c_j \mathbf{q}_j = (\boldsymbol{\psi}, \mathbf{v}, \mathbf{b})^{\mathrm{T}}\mathbf{c}, \tag{2.1}$$

where c_j is a complex coefficient for the jth mode $\mathbf{q}_j = (\psi_j, v_j, b_j)^{\mathrm{T}}$ (see section 6 of Part I), the summation Σ_j is over j ($=\pm1, \pm2, \ldots$), $\mathbf{c}$ is the vector composed of c_j, ($\boldsymbol{\psi}$, $\mathbf{v}$, $\mathbf{b}$) are the vectors composed of (ψ_j, v_j, b_j), and $(\cdot)^{\mathrm{T}}$ denotes the transpose of $(\cdot)$. As in sections 5 and 6 of Part I, the mode is numbered by $j = 2(n-1)\mathrm{sgn}(m) + m$, where n ($=1, 2, \ldots$) is the vertical mode number n ($=1, 2, \ldots$) and m ($=\pm1, \pm2$) is the root number for the four roots ($\pm\sigma_+, \pm\sigma_-$). It is easy to see that $j = -j'$ is equivalent to $n = n'$ and $m = -m'$, so $\sigma_{-j} = -\sigma_j$, $\beta_{-j} = \beta_j$, and $\psi_{-j} = -\psi_j$. By neglecting high-order vertical modes of $n > N$, the summation in (2.1) is truncated to $|j| \le 4N$.

By using $(u, w) = (\partial_z\psi, -\partial_x\psi)$ defined in (2.4b)–(2.4c) of Part I, the nonmodal solution in (2.1) can be written into

$$(u, w, v, b)^{\mathrm{T}} = (\mathbf{u}, \mathbf{w}, \mathbf{v}, \mathbf{b})^{\mathrm{T}}\mathbf{c}, \tag{2.2}$$

where ($\mathbf{u}$, $\mathbf{w}$, $\mathbf{v}$, $\mathbf{b}$) are the vectors composed of $(u_j, w_j, v_j, b_j)^{\mathrm{T}}$. Substituting (2.2) into the squared norm defined by the averaged total perturbation energy [see (4.4) and (6.3) of Part I] gives

$$\|\mathbf{q}\|_E^2 = \{E(t)\} = \mathbf{c}^{\mathrm{H}}\mathbf{A}(t)\mathbf{c}, \tag{2.3}$$

where $\mathbf{A}(t) = \{\langle \mathbf{u}^*\mathbf{u}^{\mathrm{T}} + a^2\mathbf{w}^*\mathbf{w}^{\mathrm{T}} + \mathbf{v}^*\mathbf{v}^{\mathrm{T}} + \mathbf{b}^*\mathbf{b}^{\mathrm{T}}\mathrm{Ri}\rangle\}/2$ is a matrix function of t, $(\cdot)^*$ denotes the complex conjugate of $(\cdot)$, $(\cdot)^{\mathrm{H}} = (\cdot)^{*\mathrm{T}}$ the Hermit transpose of $(\cdot)$, and $\{(\cdot)\}$ the area average of $(\cdot)$ in the cross-band vertical section over one wavelength. The normal modes in (2.2) are not orthogonal, so $\mathbf{A}(t)$ contains nondiagonal terms. This implies that the nonmodal energy growths can be larger than the modal growths. The nonmodal energy growth from $t = 0$ to a specified optimization time $t = \tau$ is measured by

$$\lambda = \lambda(\tau) = \{E(\tau)\}/\{E(0)\} = \mathbf{c}^{\mathrm{H}}\mathbf{A}(\tau)\mathbf{c}[\mathbf{c}^{\mathrm{H}}\mathbf{A}(0)\mathbf{c}]^{-1}. \tag{2.4}$$

The energy growth is maximized when $\mathbf{c}$ is the eigenvector associated with the largest eigenvalue of the following eigenvalue problem:

$$[\mathbf{A}(\tau) - \lambda\mathbf{A}(0)]\mathbf{c} = 0. \tag{2.5}$$

The largest eigenvalue is denoted by $\lambda_{\max}$, The square root of $\lambda_{\max}$ is called the leading singular value, while the associated eigenvector is called the leading singular vector and is denoted by $\mathbf{c}_{\mathrm{ls}}$. The solution given by $(u, w, v, b)^{\mathrm{T}} = (\mathbf{u}, \mathbf{w}, \mathbf{v}, \mathbf{b})^{\mathrm{T}}\mathbf{c}_{\mathrm{ls}}$ is called the leading singular perturbation that has the maximum energy growth at the optimization time $t = \tau$.

In the presence of paired growing and decaying modes, the matrix $\mathbf{A}(\tau)$ in the eigenvalue problem in (2.5) can become ill-conditioned and sometimes cause computational failures (especially when the optimization time τ is large). To avoid this problem, the decaying modes are excluded from the summation in (2.1) for the computations in the next section, so the actual truncation number is $4N - N_d$ where N_d is the number of decaying modes [see (3.5) of Part I]. This will affect the results in the next section only if the parameter point (l, Ri) is inside the unstable region. The effects of decaying modes on nonmodal growths will be examined in section 4b.

3. Nonmodal growths computed in truncated normal mode space

In this section, we will obtain numerical solutions for the eigenvalue problem formulated in the previous sec-

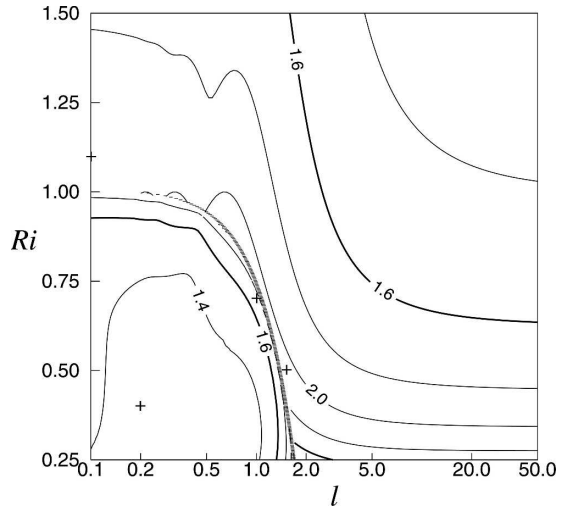

FIG. 1. Contours of scaled largest eigenvalue λ_{max} $\exp(-2\mathrm{Re}\sigma_1\tau)$ plotted every 0.2 in the parameter space of (l, Ri) for $\tau = 0.5$. Here $\mathrm{Re}\sigma_1$ is the real part of $\sigma_1 = \sigma_+$ (1), so $\mathrm{Re}\sigma_1 = \sigma_{max}$ in the unstable region and $\mathrm{Re}\sigma_1 = 0$ in the stable region (see Fig. 1a of Part I). The plus signs mark the parameter points at (l, Ri) = (0.2, 0.4) for case 1, (1.0, 0.7) for case 2, (1.5, 0.5) for case 3, and (0.1, 1.1) for case 4. These four parameter points are the same as those marked in Fig. 1a of Part I.

tion and examine the obtained maximum nonmodal energy growths for four typical cases. The complex eigenvalue problem in (2.5) is solved by the Cholesky method with N selected consecutively from 8 to 20. The results are found to become nearly independent of N as N increases to 15 and beyond, so $N = 15$ is selected for the computations presented in this section. The computed λ_{max} is scaled by $\exp(2\mathrm{Re}\sigma_1\tau)$ and plotted in Fig. 1 for $\tau = 0.5$, where $\mathrm{Re}\sigma_1$ is the real part of $\sigma_1 = \sigma_+(1)$. Note that $\mathrm{Re}\sigma_1 = \sigma_{max}$ and $\exp(2\mathrm{Re}\sigma_1\tau)$ is the energy growth produced by the fastest growing mode if the parameter point (l, Ri) is inside the unstable region [determined by $\mathrm{Ri} < 1 - (l/2)^2$ as shown in Fig. 1a of Part I]. Outside the unstable region, $\mathrm{Re}\sigma_1 = 0$ and $\exp(2\mathrm{Re}\sigma_1\tau) = 1$. As shown in Fig. 1, when the optimization time is relatively short ($\tau = 0.5$, corresponding to $0.5/f \approx 1.5$ h), the scaled maximum nonmodal growth $\lambda_{max}\exp(-2\mathrm{Re}\sigma_1\tau)$ is in the range between 1.3 and 2.5. As the optimization time increases (to 1.0 and then to 5.0), the computed nonmodal growth increases sharply (not shown) near and along the boundary outside the unstable region. Inside the unstable region, however, since the decaying modes are excluded (see section 4b for the effect of decaying modes), the asymptotic limit of the computed nonmodal growth is only slightly larger the fastest modal growth and thus the asymptotic limit of the scaled nonmodal growth is slightly larger than 1 as $\tau \to \infty$ (see Fig. 2). As mentioned in the

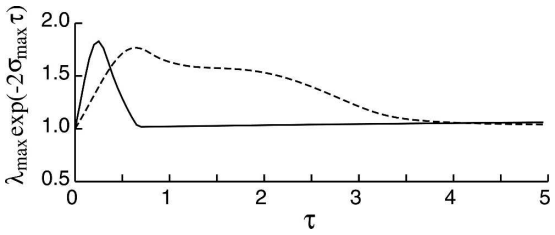

FIG. 2. Plot of $\lambda_{max}\exp(-2\sigma_{max}\tau)$ as functions of τ for case 1 (solid) and case 2 (dashed). Here $\sigma_{max} = 1.14$ for case 1 and $\sigma_{max} = 0.20$ for case 2.

introduction, we are mainly interested in nonmodal growths in the mesoscale time range. The concerned question is whether the nonmodal growth can be significantly faster than the fastest modal growth for a given τ in the mesoscale time range if the parameter point (l, Ri) is inside the unstable region. If the parameter point (l, Ri) is outside the unstable region, then the concerned question is whether and how much the nonmodal perturbations can grow for a given τ. These questions are examined for four typical cases in the following subsections. The parameter point (l, Ri) is marked in Fig. 1 for each of the four cases. The four parameter points marked in Fig. 1 are the same as those marked in Fig. 1a of Part I.

a. Case 1

The parameter point for case 1 is at (l, Ri) = (0.2, 0.4), which is well within the unstable region (see Fig. 1a of Part I). With this parameter setting, as shown by the solid curve in Fig. 2, the nonmodal growth λ_{max} can be significantly larger than the modal growth $\exp(2\sigma_{max}\tau)$ only when the optimization time τ is in the vicinity of 0.25 (about $0.25/f \approx 0.8$ h). When $\tau \leq 0.25$, the nonmodal perturbation is dominated by the paired fastest propagating modes (with $j = \pm 2$ corresponding to $n = 1$ and $m = \pm 2$). To quantify this, we need to normalize the singular perturbation and the normal modes by their respective norms at the initial time. This gives $\|\mathbf{q}(0)\|_E = 1$ and $\|\mathbf{q}_j(0)\|_E = 1$ for all j, where $\mathbf{q}(0)$ and $\mathbf{q}_j(0)$ denote the normalized singular perturbation and the jth normalized mode at $t = 0$, respectively. Note that the same symbol $\mathbf{q}_j$ has been used to denote the original nonnormalized jth mode in (2.1) but now it is used to denote the jth normalized mode in this section. The coefficient for the jth normalized mode is the product of the original jth coefficient and the initial norm of the nonnormalized jth mode, and this (product) coefficient is denoted by the same symbol c_j to simplify the notation in this section.

As shown in Table 1, when $\tau \leq 0.25$, $|c_{\pm 2}|^2$ are much

TABLE 1. Squared absolute values of coefficients for the normalized modes that are dominant or significant (with $|c_j|^2 > 0.1$) at least once in the listed optimization time range (from $\tau = 0.1$ to 1.0) for case 1. Listed in the top box of each column are the mode number j (line 1), growth rate σ_j or frequency $\omega_j = \sigma_j/i$ (line 2), and $\cos\alpha_j$ (line 3) [see (3.1)]. Since $|c_{+j}|^2 = |c_{-j}|^2$ for paired propagating modes, they are listed as $|c_{\pm j}|^2$ in the same column.

	$j = 1$	$j = \pm 2$	$j = \pm 4$	$j = \pm 6$	$j = \pm 8$	$j = \pm 15$
	$\sigma_1 = 1.14$	$\omega_{\pm 2} = \pm 5.0$	$\omega_{\pm 4} = 3.35$	$\omega_{\pm 6} = 2.60$	$\omega_{\pm 8} = 2.20$	$\omega_{\pm 15} = 0.16$
	$\cos\alpha_1 = 0.99$	$\cos\alpha_{\pm 2} = 0.96$	$\cos\alpha_{\pm 4} = 0.96$	$\cos\alpha_{\pm 6} = 0.95$	$\cos\alpha_{\pm 8} = 0.93$	$\cos\alpha_{\pm 15} = 0.03$
τ	$\lvert c_1\rvert^2$	$\lvert c_{\pm 2}\rvert^2$	$\lvert c_{\pm 4}\rvert^2$	$\lvert c_{\pm 6}\rvert^2$	$\lvert c_{\pm 8}\rvert^2$	$\lvert c_{\pm 15}\rvert^2$
0.1	0.000	0.814	0.038	0.010	0.005	0.001
0.25	0.000	0.855	0.098	0.029	0.012	0.005
0.5	0.011	0.028	0.279	0.193	0.107	0.160
0.75	1.027	0.000	0.000	0.000	0.000	0.033
1.0	1.048	0.000	0.000	0.000	0.000	0.023

larger than the sum of all the remaining $|c_j|^2$, so the paired fastest propagating modes ($j = \pm 2$) are clearly the dominant components in the leading singular perturbation. Note also that $|c_{+2}|^2 + |c_{-2}|^2$ (≈ 1.7) is significantly larger than 1 for $\tau \leq 0.25$. This result implies that the modes are not orthogonal and especially the two paired fastest propagating modes are not orthogonal to each other (as shown in Part I), because with $\|\mathbf{q}(0)\|_E = 1$ and $\|\mathbf{q}_j(0)\|_E = 1$, we would expect $\Sigma_j|c_j|^2 = 1$ if the modes were orthogonal. The above result also implies that the two paired fastest propagating modes have large amplitudes but partially offset each other initially in the leading singular perturbation for $\tau \leq 0.25$. This feature and related physical mechanism will be further examined in section 4a.

When τ increases from 0.25 to 0.5, the scaled maximum nonmodal growth decreases from 1.8 to 1.3 (see Fig. 2). In this case, $|c_{\pm 2}|^2$ decreases rapidly to 0.028, but $|c_{\pm 4}|^2$, $|c_{\pm 6}|^2$ and $|c_{\pm 8}|^2$ (for the second, third, and fourth fastest propagating modes) increase to 0.279, 0.193, and 0.107, respectively, while $|c_{\pm 15}|^2$ (the paired slowest propagating modes) increases to 0.16 (see Table 1). These four pairs ($j = \pm 4, \pm 6, \pm 8$, and ± 15) become jointly dominant as the sum of their squared absolute coefficients (=1.478) is much larger than the sum of all the remaining $|c_j|^2$ for $\tau = 0.5$. When τ increases to 0.75 and then to 1.0, $|c_1|^2$ increases rapidly to 1.027 and then to 1.048, so the fastest growing mode ($j = 1$) becomes the dominant component. Note that the decaying modes are excluded and $|c_1|^2 = 1.027$ for $\tau = 0.75$. This implies that the fastest growing mode is nearly orthogonal to the remaining modes, and only a small fraction of this mode is offset initially by the combination of the remaining modes in the leading singular perturbation. In this case, $\|\mathbf{q}(0)\|_E^2 = 1 < |c_1|^2\|\mathbf{q}_1(0)\|_E^2 = |c_1|^2$ but $\lambda_{\max} = \|\mathbf{q}(\tau)\|_E^2 \to |c_1|^2\|\mathbf{q}_1(\tau)\|_E^2 = |c_1|^2 \exp(2\sigma_{\max}\tau)$ as $\tau \to \infty$. This explains why the scaled nonmodal growth $\lambda_{\max}\exp(-2\sigma_{\max}\tau)$ (=1.019) tends to become the same as $|c_1|^2$ in the normalized leading singular vector as τ increases (to 0.75 and beyond).

In this section, the adjoint modes are also normalized by their respective norms at the initial time. This gives $\|\mathbf{q}_j^a(0)\|_E = 1$ for all j, so (6.8) of part I reduces to

$$c_j = \langle \mathbf{q}_j^a(0), \mathbf{q}(0)\rangle_E/\cos\alpha_j \quad \text{for} \quad \sigma_j \neq 0 \quad \text{or} \quad j < 0, \tag{3.1}$$

where α_j is the angle between the jth mode $\mathbf{q}_j$ and its adjoint mode $\mathbf{q}_j^a$ [see (6.10) of Part I]. As shown in Table 1, $\cos\alpha_{\pm 2}$ (=0.96) is close to 1, so $|\langle \mathbf{q}_{\pm 2}^a(0), \mathbf{q}(0)\rangle_E| = |c_{\pm 2}\cos\alpha_{\pm 2}| \approx |c_{\pm 2}|$ according to (3.1). This means that the initial projections of $\mathbf{q}_{\pm 2}^a$ on the leading singular perturbation (or vice versa) have nearly the same absolute value as $c_{\pm 2}$. Thus, the results in Table 1 imply that $\mathbf{q}_{\pm 2}$ have the largest initial projections (among all the adjoint modes) when $\tau \leq 0.25$. Similarly, $\cos\alpha_{\pm 4}$ and $\cos\alpha_{\pm 6}$ are also close to 1, and $\mathbf{q}_{\pm 4}^a$ and $\mathbf{q}_{\pm 6}^a$ have the most significant initial projections on the leading singular perturbation for $\tau = 0.5$. On the other hand, $\cos\alpha_{\pm 15}$ is very small (=0.03) for the paired slowest propagating modes, so $\mathbf{q}_{\pm 15}^a$ has a small initial projection on the leading singular perturbation even when $|c_{\pm 15}|$ reaches the maximum value of 0.4 (corresponding to $|c_{\pm 15}|^2 = 0.16$ for $\tau = 0.5$). For the fastest growing mode ($j = 1$), $\cos\alpha_1$ (=0.99) is very close to 1, so the initial projection of $\mathbf{q}_1^a$ on the leading singular perturbation has almost the same absolute value as c_1. This initial projection is the largest among all the adjoint initial projections for $\tau \geq 0.75$.

b. Case 2

The parameter point now is at (l, Ri) = (1.0, 0.7) which is still within the unstable region but near the boundary of the unstable region (see Fig. 1a of Part I). As shown by the dashed curve in Fig. 2, the nonmodal growth is significantly larger than the modal growth for

TABLE 2. As in Table 1 but for case 2.

	$j = 1$	$j = \pm 2$	$j = \pm 3$	$j = \pm 4$	$j = \pm 6$
	$\sigma_1 = 0.202$	$\omega_{\pm 2} = 2.15$	$\omega_{\pm 3} = 0.54$	$\omega_{\pm 4} = 1.55$	$\omega_{\pm 6} = 1.35$
	$\cos\alpha_1 = 0.10$	$\cos\alpha_{\pm 2} = 1.0$	$\cos\alpha_{\pm 3} = 0.43$	$\cos\alpha_{\pm 4} = 0.93$	$\cos\alpha_{\pm 6} = 0.96$
τ	$\lvert c_1\rvert^2$	$\lvert c_{\pm 2}\rvert^2$	$\lvert c_{\pm 3}\rvert^2$	$\lvert c_{\pm 4}\rvert^2$	$\lvert c_{\pm 6}\rvert^2$
0.25	0.003	0.690	0.002	0.008	0.002
0.5	0.006	0.748	0.004	0.016	0.005
0.65	0.011	0.718	0.008	0.037	0.011
0.75	0.019	0.614	0.017	0.008	0.024
1.0	0.041	0.076	0.091	0.214	0.106
2.0	0.062	0.011	0.911	0.001	0.001
3.0	0.304	0.000	0.793	0.005	0.002
4.0	0.971	0.005	0.042	0.000	0.001
5.0	1.009	0.003	0.007	0.002	0.000
10.0	1.021	0.001	0.002	0.001	0.000

a wide range of τ (up to about $3/f \approx 10$ h). The scaled nonmodal growth $\lambda_{\max}\exp(-2\sigma_{\max}\tau)$ reaches a peak value of 1.75 at $\tau = 0.65$. When τ is in the vicinity of 0.65, the leading singular perturbation is mainly composed of the paired fastest propagating modes (with $j = \pm 2$). In this case, as shown in Table 2, $|c_{+2}|^2 + |c_{-2}|^2$ ($\approx$1.5) is significantly larger that 1, so the two paired fastest propagating modes have large amplitudes but partially offset each other initially in the leading singular perturbation (for $\tau = 0.5 \pm 0.25$). This situation is similar to that in case 1. When τ increases to 1.0, $|c_{\pm 2}|^2$ reduces rapidly to 0.076, but $|c_{\pm 4}|^2$ increase to 0.214, so the second fastest propagating modes ($j = \pm 4$) become dominant. When τ increases to 2.0, $|c_{\pm 4}|^2$ drops sharply to 0.001 but $|c_{\pm 3}|^2$ increases rapidly to 0.911, so the paired slowest propagating modes ($j = \pm 3$) become dominant (for $2.0 \le \tau \le 3.0$). When τ increases to 4.0 and beyond, $|c_1|^2$ (=0.971) becomes much larger than the sum of all the remaining $|c_j|^2$, so the fastest growing mode ($j = 1$) becomes the dominant component, as shown in Table 2.

For the paired fastest propagating modes ($j = \pm 2$), we have $\cos\alpha_{\pm 2} = 1$, so $\mathbf{q}^a_{\pm 2}$ and $\mathbf{q}_{\pm 2}$ happen to be parallel in this case. Thus, the initial projections of $\mathbf{q}^a_{\pm 2}$ on the leading singular perturbation have the same absolute value as $c_{\pm 2}$ according to (3.1), and they are the largest initial adjoint projections when $\tau = 0.5 \pm 0.25$ (as implied by the results in Table 2). For the paired slowest propagating modes ($j = \pm 3$), we have $\cos\alpha_{\pm 3} = 0.43$, so the initial projections of $\mathbf{q}^a_{\pm 3}$ on the leading singular perturbation have a smaller absolute value than $|c_{\pm 3}|$. In this case, the dominance of the paired slowest propagating modes in the leading singular vector (for $2.0 \le \tau \le 3.0$) depends not only on the initial projections of $\mathbf{q}^a_{\pm 3}$ but also on the nonparallelism between $\mathbf{q}_{\pm 3}$ and $\mathbf{q}^a_{\pm 3}$ (that yields $\cos\alpha_{\pm 3} = 0.43 < 1$). For the fastest growing mode ($j = 1$), we have $\cos\alpha_1 = 0.10$, so that $|c_1|$ can be large even when $\mathbf{q}^a_1$ does not have a large initial projection on the leading singular perturbation. The reduced parallelism between $\mathbf{q}^a_1$ and $\mathbf{q}_1$ (with $\cos\alpha_1$ reduced from 0.99 in case 1 to 0.1 in this case) is caused by the reduced growth rate (with σ_1 reduced from 1.14 in case 1 to 0.2 in this case) [see the discussion after (6.10) in section 6 of Part I].

c. Case 3

The parameter point for case 3 is at (l, Ri) = (1.5, 0.5), which is near the boundary but outside the unstable region (see Fig. 1a of Part I). Since there is no growing mode, $\exp(2\mathrm{Re}\sigma_1\tau) = 1$ and the scaled growth is $\lambda_{\max}$ itself. As shown by the dashed curve in Fig. 3, $\lambda_{\max}$ increases from 1 to the maximum (35.5) as τ increases from 0 to 8.0 ($8/f \approx 24$ h), and then decreases slowly. As τ further increases (not shown), $\lambda_{\max}$ oscillates periodically between the same maximum (=35.5) and minimum (=1). The oscillations of $\lambda_{\max}$ are caused by the paired slowest propagating modes ($j = \pm 1$). In particular, as shown in Table 3, $|c_{\pm 1}|^2$ increases rapidly from 0.333 to 4.425 when τ increases from 0.5 to 1.0, and

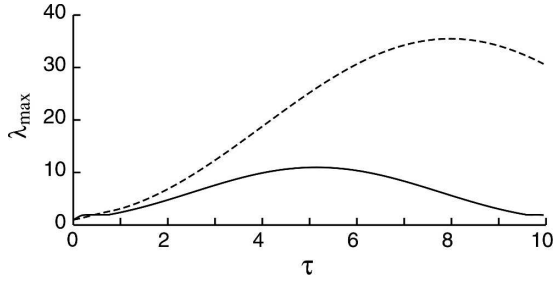

FIG. 3. Plot of $\lambda_{\max}$ as functions of τ for case 3 (dashed) and case 4 (solid).

TABLE 3. As in Table 1 except for case 3.

	$j = \pm 1$	$j = \pm 2$
	$\omega_{\pm 1} = 0.20$	$\omega_{\pm 2} = 1.68$
	$\cos\alpha_{\pm 1} = 0.06$	$\cos\alpha_{\pm 2} = 0.91$
τ	$\lvert c_{\pm 1}\rvert^2$	$\lvert c_{\pm 2}\rvert^2$
0.1	0.117	0.609
0.5	0.333	0.692
0.65	0.713	0.615
0.75	1.346	0.480
1.0	4.425	0.090
2.0	7.982	0.001
4.0	8.879	0.000
10.0	9.061	0.000

then increases to 7.982 and 9.061 when τ increases to 2 and 10, respectively. These results indicate that the nonmodal growth is produced almost solely by the paired slowest propagating modes when τ increases to 1 and beyond until τ becomes close to the oscillation period (=16, not shown but will be explained in section 4). This feature will be further quantified in section 4a. When $\tau = 0.65$, $|c_{\pm 2}|^2$ (=0.615) becomes close to $|c_{\pm 1}|^2$ (=0.713), and these two pairs ($j = \pm 1$ and ± 2) become jointly dominant because $|c_{+1}|^2 + |c_{-1}|^2 + |c_{+2}|^2 + |c_{-2}|^2$ (=2.66) is much larger than the sum of all the remaining $|c_j|^2$. When $\tau = 0.5$, $|c_{\pm 2}|^2$ (=0.692) becomes significantly larger than $|c_{\pm 1}|^2$ (=0.333), so the nonmodal growth is supported mainly by the paired fastest propagating modes. This feature (for $\tau \leq 0.5$ here) is similar to that for $\tau \leq 0.25$ in case 1 and for $\tau \leq 0.65$ in case 2.

For the paired fastest propagating modes ($j = \pm 2$), we have $\cos\alpha_{\pm 2} = 0.91$, so the initial projections of $\mathbf{q}^a_{\pm 2}$ on the leading singular perturbation have nearly the same absolute value as $c_{\pm 2}$, and they are the largest initial adjoint projections when $\tau \leq 0.5$ (as implied by the results in Table 3). For the paired slowest propagating modes ($j = \pm 1$), we have $\cos\alpha_{\pm 1} = 0.06$, so $\mathbf{q}^a_{\pm 1}$ and $\mathbf{q}_{\pm 1}$ are nearly orthogonal. This near orthogonality is caused by the reduced frequency ($\omega_1 = \sigma_1/i = 0.2$) [see (6.10) of Part I]. In this case, it is easy to see that the initial projections of $\mathbf{q}^a_{\pm 1}$ are all very small and, in particular, $\langle \mathbf{q}^a_{\pm 1}(0), \mathbf{q}(0)\rangle_E| = |c_{\pm 1}\cos\alpha_{\pm 1}| <$ or $\ll 0.2$ for the values of $|c_{\pm 1}|^2$ listed in Table 3.

d. Case 4

For case 4, the parameter point is at (l, Ri) = (0.1, 1.1) on the short-wave side above the unstable region (see Fig. 1). The nonmodal growth (shown by the solid curve in Fig. 3) and related features are similar to those in case 3 but the amplitude and period of the oscillations are reduced. As in case 3, the oscillations of λ_{max} are also caused mainly by the paired slowest propagating modes (with $j = \pm 1$), but the paired slowest propagating modes are not as dominant as those for $2 < \tau < 14$ in case 3. In the current case, the two slowest propagating modes are dominant components for $0.8 < \tau < 9.6$. This range of τ covers nearly the entire oscillation period ($0 < \tau < 10$) of λ_{max}. When τ decreases from 0.3 to 0.2, the paired fastest propagating modes become increasingly significant. When $\tau \leq 0.2$, the nonmodal growth is produced dominantly by the paired fastest propagating modes. The situation is similar to that for $\tau \leq 0.5$ in case 3, but the dominance of the paired fastest propagating modes is stronger than that in case 3.

4. Nonmodal growths produced by paired modes

a. Paired propagating modes

As we can see from the four cases examined in the previous section, when τ is sufficiently small, the maximum energy growth is produced dominantly by the paired fastest propagating modes. When the parameter point (l, Ri) is near the boundary inside the unstable region, as shown in case 2, the paired slowest propagating modes can contribute significantly to the nonmodal energy growth before the fastest growing mode becomes dominant. When the parameter point (l, Ri) is near the boundary outside the unstable region, as shown in case 3, the maximum energy growth is produced almost solely by the paired slowest propagating modes for a wide range of optimization time τ. To understand the physical mechanisms of the nonmodal energy growths produced by paired propagating modes, we need to analyze the eigenvalue problem (2.5) in the subspace spanned by a pair of propagating modes in this section.

Consider a pair of propagating modes, say, the jth pair composed of the jth and j'th modes with $j = -j' > 0$. As explained in section 6 of Part I, these two modes have the same, exactly in-phase, spatial structures in (u, w) but the opposite, exactly 180° out-of-phase, spatial structures in (v, b). These two modes propagate in opposite horizontal directions and their phase speeds are given by ω_j/k (>0) and $\omega_{j'}/k = -\omega_j/k$ (<0), respectively, where $\omega_j = \sigma_j/i$ and $\omega_{j'} = \sigma_{j'}/i$ are their respective frequencies. Denote by $\mathbf{A}_j(t)$ the 2×2 submatrix of $\mathbf{A}(t)$ associated with the jth subspace spanned by the jth and j'th modes with $j = -j' > 0$. By using the analytical form of the normal mode solution in (3.6)/σ_j of Part I, one can show that $\mathbf{A}_j(t)$ has the following form:

$$\mathbf{A}_j(t) = X_j\begin{pmatrix} 1 & \exp(i2\omega_j t) \\ \exp(-i2\omega_j t) & 1 \end{pmatrix} + Y_j\begin{pmatrix} 1 & -\exp(i2\omega_j t) \\ -\exp(-i2\omega_j t) & 1 \end{pmatrix}, \tag{4.1}$$

where

$$X_j = \{|u_j|^2 + a^2|w_j|^2\}/2 = [(n\pi)^2 + (a^2 + \beta_j^2)k^2]/4, \tag{4.2a}$$

$$Y_j = \{|\upsilon_j|^2 + \mathrm{Ri}|b_j|^2\}/2 = Z_j/|\omega_j|^2, \tag{4.2b}$$

$$Z_j = [X_j + (\mathrm{Ri} - a^2)k^2/4](1 + \mathrm{Ri}^{-1}) - \beta_j k^2. \tag{4.2c}$$

Here $\omega_j = -\omega_{j'} > 0$, $\beta_j = \beta_{j'}$ and the aforementioned opposite polarization relationships between the two paired propagating modes are used in the derivation of (4.1)–(4.2). Note that X_j and Z_j are the same as those in (5.5) and (6.10) of Part I. According to the energy terms defined in (4.3) of Part I, X_j is given by $\{K_2\}$ with $(u, w) = (u_j, w_j)$ and Y_j is given by $\{K_\upsilon + P_b\}$ with $(\upsilon, b) = (\upsilon_j, b_j)$, so X_j is the cross-band kinetic energy and Y_j is the along-band kinetic energy plus the buoyancy energy for the jth mode at the initial time. In the jth subspace, the eigenvalue problem in (2.5) reduces to

$$[\mathbf{A}_j(\tau) - \lambda_j \mathbf{A}_j(0)]\mathbf{c}_j = 0, \tag{4.3}$$

where $\mathbf{c}_j = (c_j, c_{j'})^{\mathrm{T}} = (c_j, c_{-j})^{\mathrm{T}}$ is the vector coefficient for the jth and j'th modes and $(\cdot)^{\mathrm{T}}$ denotes the transpose of $(\cdot)$. Here, λ_j denotes the eigenvalue in the jth subspace. Since the solution will be considered only in the subspace, the subscript j will be dropped from λ_j as long as the meaning is clearly understood. If the nonmodal growth is produced dominantly by the jth pair, then the largest eigenvalue obtained from (4.3) should be a good approximation of that obtained from (2.5). In this case, the problem is greatly simplified and can be examined analytically.

As shown by (A.7) in appendix A, (4.3) has two eigenvalues given by

$$\lambda_\pm = q_j \pm (q_j^2 - 1)^{1/2}, \tag{4.4}$$

where

$$q_j = [1 - \gamma^2 \cos(2\omega_j\tau)]/(1 - \gamma^2) \tag{4.5}$$

$$\text{and} \quad \gamma = (X_j - Y_j)/(X_j + Y_j). \tag{4.6}$$

Clearly, q_j and $\lambda_\pm$ are periodic functions of τ. The function forms of λ_+ are plotted in Fig. 4 for different values of γ^2 (=0, 0.2, 0.4, 0.6, 0.8) over one period ($0 \le 2\omega_j\tau \le 2\pi$). As shown in appendix A, when $\tau = 0$, the two eigenvalues collapse into $\lambda_\pm = 1$ and the associated eigenvectors become arbitrary. This result is trivial and is consistent with the fact that the normalized energy is unity for $\tau = 0$ according to (2.4). When τ increases from 0 to $\pi/(2\omega_j)$, λ_+ increases from 1 to $\max(X_j/Y_j, Y_j/X_j)$ and λ_- decreases from 1 to $\min(X_j/Y_j, Y_j/X_j)$. Thus, as long as $X_j \neq Y_j$, a nonmodal energy growth can be caused by the paired propagating modes and the maximum growth is $\lambda_+ = \max(X_j/Y_j, Y_j/X_j)$ as $\tau = \pi/(2\omega_j)$. In this case, as shown in appendix A, the associated eigenvector is given by $\mathbf{c}_j = (c_j, c_{j'})^{\mathrm{T}} \propto (1, -1)^{\mathrm{T}}$ if $X_j > Y_j$ or by $\mathbf{c}_j = (c_j, c_{j'})^{\mathrm{T}} \propto (1, 1)^{\mathrm{T}}$ if $X_j < Y_j$. However, if $X_j = Y_j$, then $\gamma = 0$ and the eigenvalue problem in (4.3) becomes trivial. In this case, $\lambda_+ = \lambda_- = 1$, so the paired propagating modes produce no energy growth. This occurs for the paired slowly propagating modes (with $m = \pm 1$ for a give n) only when the parameter point (nl, Ri) is on the zero γ contour (in the domain of $\mathrm{Ri} > 1$ outside the unstable region) in Fig. 5a. For the paired fast propagating modes (with $m = \pm 2$ for a give n), γ is nonzero and negative (see Fig. 5b), so $\lambda_+ = Y_j/X_j > 1$ as $\tau = \pi/(2\omega_j)$.

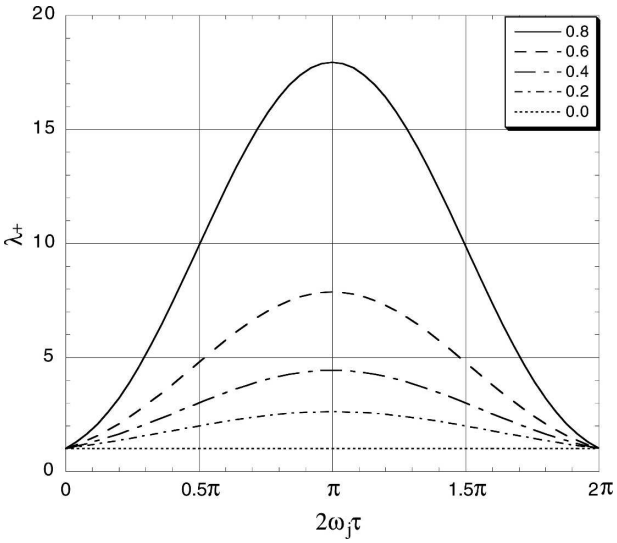

FIG. 4. Plot of λ_+ for different values of γ^2 (=0, 0.2, 0.4, 0.6, 0.8) over one period ($0 \le 2\omega_j\tau \le 2\pi$). Here λ_+ is the largest eigenvalue in the subspace spanned by a pair of propagating modes (represented by the jth and j'th modes with $j = -j' > 0$), and $\omega_j > 0$ is the frequency of the (jth) propagating mode.

The asymptotic behaviors of X_j/Y_j and γ are examined in appendix B for the limiting cases of $nl \to \infty$ [see (B.1)–(B.2)], $nl \to 0$ [see (B.3)–(B.5)], $\mathrm{Ri} \to 1$ [see (B.6)–(B.9)] and $\mathrm{Ri} \to \infty$ [see (B.10)–(B.11)]. As shown in (B.9), $Y_j/X_j = 2$ for $\mathrm{Ri} = 1$, and this gives $\gamma = -1/3$ for all paired propagating modes as shown in Figs. 5a and 5b. When Ri moves away from 1 (in the range of $0.25 \le \mathrm{Ri} \le 1.5$), Y_j/X_j and γ become increasingly dependent on l for the paired slowly propagating modes

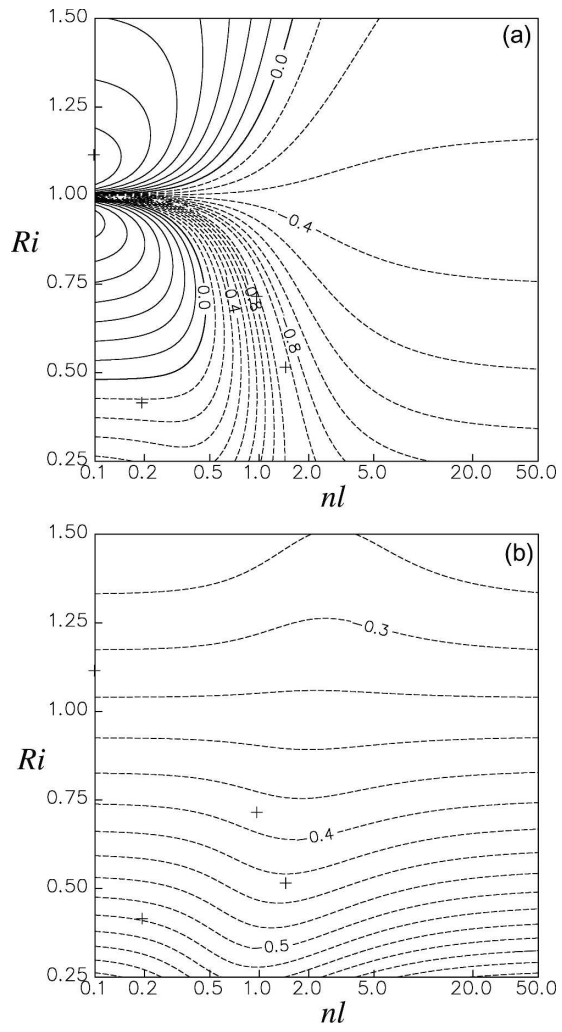

FIG. 5. Plot of $\gamma = (X_j - Y_j)/(X_j + Y_j)$ [see (4.6)] as functions of (nl, Ri) for a given n with (a) $m = \pm 1$ and thus $j = \pm[2(n-1)+1]$, and (b) $m = \pm 2$ and thus $j = \pm[2(n-1)+2]$. When $n = 1$, the plotted results are for the paired slowest propagating modes or paired fastest growing and decaying modes (with $j = \pm 1$) in (a) and for the paired fastest propagating modes (with $j = \pm 2$) in (b). For a given n, the boundary of the unstable region is defined by $\mathrm{Ri} = 1 - (nl/2)^2$ and is shown by the zero contour of σ_+^2 in Fig. 1a of Part I. This boundary (not shown) is between the two contours of $\gamma = -0.9$ in (a). At this boundary, γ reaches the minimum value of -1 (not shown) in (a).

(see Fig. 5a) but remain to be nearly independent of l for the paired fast propagating modes (see Fig. 5b). Clearly, Y_j/X_j has very different wavelength dependencies for the two types of modes, and this can be explained as follows. As shown in Part I, for a slowly propagating mode, the cross-band circulation is tilted more slantwise than the M surface and B surface, so the mode propagation is driven by the inertial restoring force but slowed by the buoyancy restoring force. Because of this, the wave frequency can approach zero and the polarization relationships (and thus Y_j/X_j) can become increasingly singular as $nl \to 2(1 - \mathrm{Ri})^{1/2}$. For a fast propagating mode, the cross-band circulation is tilted in the opposite direction with respect to the M surface and B surface, so the mode propagation is driven by both the inertial and buoyancy restoring forces, and this driving mechanism is qualitatively the same as that for the classic inertial gravity waves in uniformly stratified nonsheared basic flows. For the latter, we have $Y_j/X_j = 1$ and $\gamma = -1$ independent of the wavelength l [see (B.11)]. Because the fast propagating modes are driven nearly by the same mechanism as the classic inertial gravity waves, their energy partitions between X and Y_j are nearly independent of l. This explains the aforementioned difference between Figs. 5b and 5a.

As explained at the beginning of this section, the two paired propagating modes have exactly opposite polarization relationships between ψ and (v, b). As the two modes propagate toward each other in opposite horizontal directions, their associated ψ and (u, w) fields become exactly in phase (or out of phase) when their associated (v, b) fields become exactly out of phase (or in phase). Thus, the composed (v, b) fields oscillate with the same frequency ω_j as the composed (u, w) fields, but the oscillations of the (v, b) fields are 90° out of phase with respect to the oscillations of the (u, w) fields. Note that $\{K_2\}$ and $\{K_v + P_b\}$ are integrated squares of (u, w) and (v, b), respectively, so they oscillate between zero and their respective maxima with the same frequency ($=2\omega_j$) and the phase difference between the oscillations of $\{K_2\}$ and $\{K_v + P_b\}$ is just 180°. Since the amplitudes of the composed (u, w) and (v, b) are twice of those for the jth or j'th mode, the maxima of $\{K_2\}$ and $\{K_v + P_b\}$ are $4X_j$ and $4Y_j$, respectively. When $X_j = Y_j$, the oscillation of $\{K_2\}$ offsets the oscillation of $\{K_v + P_b\}$, so the total energy $\{E\} = \{K_2 + K_v + P_b\}$ keeps constant in time. This explains why the paired propagating modes produce no energy growth (i.e., $\lambda_+ = \lambda_- = 1$) when $X_j = Y_j$.

However, when $X_j > Y_j$ (or $X_j < Y_j$), the oscillation of $\{K_2\}$ (or $\{K_v + P_b\}$) becomes dominant and thus the total energy oscillates between $4Y_j \le \{E\} \le 4X_j$, (or $4X_j \le \{E\} \le 4Y_j$). In particular, if $X_j > Y_j$ and $\mathbf{c}_j \propto (1, -1)^{\mathrm{T}}$, then $\{K_2\} = 0$ and thus $\{E\} = \{K_v + P_b\} = 4Y_j$ at $t = 0$. As t increases from 0 to $\pi/2\omega_j$ (i.e., one quarter of the wave period of the jth mode), $\{K_2\}$ increases from 0 to the maximum ($=4X_j$) but $\{K_v + P_b\}$ decreases from the maximum ($=4Y_j$) to 0, so $\{E\}$ increases maximally from $4Y_j$ to $4X_j$. Similarly, if $X_j < Y_j$ and $\mathbf{c}_j \propto (1, 1)^{\mathrm{T}}$, then $\{E\}$ increases maximally from $4X_j$ to $4Y_j$ as t increases from 0 to $\pi/2\omega_j$. This explains why and how the paired propagating modes produce the energy growth

of $\lambda_+ = X_j/Y_j$ for $X_j > Y_j$ (or $\lambda_+ = Y_j/X_j$ for $X_j < Y_j$) as t increases from 0 to $\tau = \pi/2\omega_j$. Note from (4.2) that Y_j/X_j is proportional to ω_j^{-2}, so λ_+ can be very large when ω_j is very small, as seen from the paired slowest propagating modes in case 3. Based on the above analysis and physical understanding, the numerical results presented in section 3 can be examined in terms of optimal combinations of paired propagating modes as follows.

For the paired fastest propagating modes (with j = ±2) in case 1, we have $\omega_j = 5.01$ and $Y_j/X_j = 3.25$. According to (4.4), the maximum energy growth produced by these two fastest propagating modes reaches $\lambda_+ = Y_j/X_j = 3.25$ as $\tau = \pi/(2\omega_j) = 0.31$. Note that $\sigma_{\max} = \sigma_1 = 1.14$, so $\exp(2\sigma_{\max}\tau) = 2.05$ and the scaled growth is $\lambda_+ \exp(2\sigma_{\max}\tau) = 1.56$. This value (1.56 at $\tau =$ 0.31) is reasonably close to the maximum of 1.8 at $\tau =$ 0.25 for the solid curve in Fig. 2. Thus, as assessed in section 3a, the nonmodal energy growth is produced mainly by the paired fastest propagating modes when τ is small (≤0.25). The related physical mechanism is further quantified analytically in this section.

For the paired fastest propagating modes (with $j =$ ±2) in case 2, we have $\omega_j = 2.15$ and $Y_j/X_j = 2.28$. The maximum energy growth produced by these two fastest propagating modes reaches $\lambda_+ = Y_j/X_j = 2.28$ as $\tau =$ $\pi/(2\omega_j) = 0.73$. Note that $\sigma_{\max} = \sigma_1 = 0.20$, so $\exp(2\sigma_{\max}\tau) = 1.34$ and the scaled growth is λ_+ $\exp(2\sigma_{\max}\tau) = 1.70$. This value (1.70 at $\tau = 0.73$) is very close to the maximum of 1.75 at $\tau = 0.7$ for the dashed curve in Fig. 2. Thus, as assessed in section 3b, the nonmodal growth is produced mainly by the paired fastest propagating modes as τ is small (≤0.75), and this is further quantified here.

For the paired slowest propagating modes (with $j =$ ±1) in case 3, we have $\omega_j = 0.20$ and $Y_j/X_j = 35.45$. The maximum energy growth produced by these two slowest propagating modes reaches $\lambda_+ = Y_j/X_j = 35.45$ as $\tau = \pi/(2\omega_j) = 8.0$. This value (35.45 at $\tau = 8.0$) is extremely close to the maximum of the dashed curve in Fig. 3. Thus, as assessed in section 3c and further quantified here, the nonmodal growth is produced almost completely by the paired slowest propagating modes for a wide range of optimization time ($2 < \tau < 14$) within the oscillation period ($0 < \tau < 16$) of $\lambda_{\max}$.

For the paired slowest propagating modes (with $j =$ ±1) in case 4, we have $\omega_j = 0.30$ and $X_j/Y_j = 7.6$. The maximum energy growth produced by these two slowest propagating modes reaches $\lambda_+ = X_j/Y_j = 7.6$ as $\tau =$ $\pi/(2\omega_j) = 5.2$. This value ($\lambda_+ = 7.6$ at $\tau = 5.2$) is close to the maximum of the solid curve at $\tau = 5.15$ in Fig. 3. Thus, the nonmodal growth is produced mostly by the paired slowest propagating modes for a wide range of optimization time ($0.8 < \tau < 9.6$) within the oscillation period ($0 < \tau < 10.4$) of $\lambda_{\max}$.

b. Paired growing and decaying modes

As mentioned in section 2, in the presence of paired growing and decaying modes, the eigenvalue problem in (2.5) can become ill conditioned, especially when τ is large. This problem is avoided by excluding the decaying modes from the summation in (2.1). The effects of decaying modes on nonmodal growths, however, are not always negligible. As explained at the beginning of section 2, any two paired modes (with $j = -j' > 0$) have the opposite polarization relationships between ψ and (u, b). This implies that the fastest decaying mode can be combined with the fastest growing mode to reduce the initial total perturbation energy $\{E(0)\}$. As the time increases, the decaying mode decreases monotonically. The nonmodal energy growth measured by $\{E(\tau)\}/\{E(0)\}$ in (2.4) is thus enhanced due to the inclusion of the decaying mode. To quantify this mechanism and the related energy growth, we need to analyze the eigenvalue problem (2.5) in the subspace spanned by a pair of growing and decaying modes.

Consider a pair of growing and decaying modes, say, the jth pair. Denote by $\mathbf{A}_j(t)$ the 2×2 submatrix of $\mathbf{A}(t)$ associated with the jth subspace spanned by the jth pair of modes (with $j = -j' > 0$). By using (3.6)/σ_j of Part I with the aforementioned polarization relationships, one can show that

$$\mathbf{A}_j(t) = X_j \begin{pmatrix} \exp(2\sigma_j t) & 1 \\ 1 & \exp(-2\sigma_j t) \end{pmatrix} + Y_j \begin{pmatrix} \exp(2\sigma_j t) & -1 \\ -1 & \exp(-2\sigma_j t) \end{pmatrix}, \quad (4.7)$$

where X_j and Y_j are as in (4.2) and $|\omega_j| = |\sigma_j| = \sigma_j = -\sigma_{j'} > 0$. In the jth subspace, the eigenvalue problem in (2.5) reduces to (4.3) but with $\mathbf{A}_j(\tau)$ and $\mathbf{A}_j(0)$ given by (4.7) instead of (4.1). The reduced eigenvalue problem has two eigenvalues given by $\lambda_\pm = q_j \pm (q_j^2 - 1)^{1/2}$ as in (4.4) but with

$$q_j = [\cosh(2\sigma_j\tau) - \gamma^2]/(1 - \gamma^2), \quad (4.8)$$

where γ is as in (4.6). The derivation of (4.8) is similar to that for (4.5) in appendix A, but the details are omitted. If $X_j = Y_j$, then $\gamma = 0$ and the two eigenvalues reduce to $\lambda_\pm = \exp(\pm 2\sigma_j\tau)$. In this case, the energy growth is supported solely by the growing mode and thus is not affected by the decaying mode. This occurs only when the parameter point (nl, Ri) is on the zero γ-contour line inside the unstable region as shown in Fig. 5a for the paired growing and decaying modes

(with a given n). Away from the zero γ-contour line, $X_j \neq Y_j$ and $(1 - \gamma^2)^{-1} = 1 + (X_j - Y_j)^2/(4X_jY_j) > 1$ within the unstable region. In this case, as shown in Fig. 6, the scaled nonmodal growth, defined by $\lambda_+ \exp(-2\sigma_j\tau)$, increases monotonically from 1 toward the asymptotic limit of $(1 - \gamma^2)^{-1}$ as τ increases from 0 toward infinity.

The eigenvector associated with λ_+ is given by $\mathbf{c}_j = (c_j, c_{j'})^{\mathrm{T}} \propto (1, -\gamma)^{\mathrm{T}} \propto (X_j + Y_j, Y_j - X_j)^{\mathrm{T}}$. By setting $c_j = X_j + Y_j$ and $c_{j'} = Y_j - X_j$, the initial nonmodal fields are given by $c_j(u_j, w_j) + c_{j'}(u_{j'}, w_{j'}) = 2Y_j(u_j, w_j)$ and $c_j(v_j, b_j) + c_{j'}(v_{j'}, b_{j'}) = 2X_j(v_j, b_j)$, so the initial total energy is $\{E(0)\} = \{K_2 + K_v + P_b\} = (2Y_j)^2X_j + (2X_j)^2Y_j = 4X_jY_j(X_j + Y_j)$ according to (2.3), (4.2), and (4.7). The initial total energy for the growing mode only, however, is $c_j^2(X_j + Y_j) = (X_j + Y_j)^2(X_j + Y_j)$. Thus, the total energy is reduced at the initial time by a factor of $4X_jY_j(X_j + Y_j)^{-2} = 1 - \gamma^2$ (<1) due to the inclusion of the decaying mode. Thus, as $t \to \tau \to \infty$, the decaying mode diminishes and $\exp(-2\sigma_j\tau)\{E(\tau)\}/\{E(0)\} \to (X_j + Y_j)^2(4X_jY_j)^{-1} = (1 - \gamma^2)^{-1}$. This is precisely the above derived asymptotic limit of the scaled nonmodal growth (see Fig. 6).

In the above analysis, $c_j = X_j + Y_j$ is the coefficient for the growing mode and is positive, while $c_{j'} = Y_j - X_j$ is the coefficient for the decaying mode. Note that $(u_j, w_j) = (u_{j'}, w_{j'})$ and $(v_j, b_j) = -(v_{j'}, b_{j'})$. When $X_j > Y_j$, $c_{j'}$ is negative, the initial field $c_{j'}(u_{j'}, w_{j'})$ for the decaying mode and the initial field $c_j(u_j, w_j)$ for the growing mode are out of phase. This causes a decrease in $\{K_2\}$ that excessively offsets the increase in $\{K_v + P_b\}$ caused by the in-phase relationship between $c_j(v_j, b_j)$ and $c_{j'}(v_{j'}, b_{j'})$ at the initial time. When $X_j < Y_j$, $c_{j'}$ is positive, so $c_j(v_j, b_j)$ and $c_{j'}(v_{j'}, b_{j'})$ are out of phase initially. This causes a decrease in $\{K_v + P_b\}$ that excessively offsets the increase in $\{K_2\}$ caused by the in-phase relationship between $c_{j'}(u_{j'}, w_{j'})$ and $c_j(u_j, w_j)$ at the initial time. Thus, when $X_j \neq Y_j$, the decaying mode can reduce the initial total energy and enhance the nonmodal growth.

The above analytical results can be used to evaluate how the results for case 1 and case 2 in Fig. 2 will be affected if the decaying modes are included in the solutions. For case 1, we have $\sigma_1 = \sigma_{\max} = 1.14$. As discussed in section 3a, the nonmodal growth is dominated by the fastest growing mode when $\tau > 0.65$ ($\sigma_1\tau > 0.74$). In this case, since $\gamma^2 = 0.02$ and $(1 - \gamma^2)^{-1} = 1.02$ for the paired fastest growing and decaying modes, the scaled nonmodal growth (shown by the solid curve in Fig. 2) is increased only 2% (by adding the fastest decaying mode) even when τ approaches infinity. When $\tau < 0.65$ (or $\sigma_1\tau < 0.74$), the nonmodal growth is produced mainly by paired propagating modes (as discussed in sections 3a and 4a) and is not affected by the decaying modes. Thus, the decaying modes can be neglected for case 1.

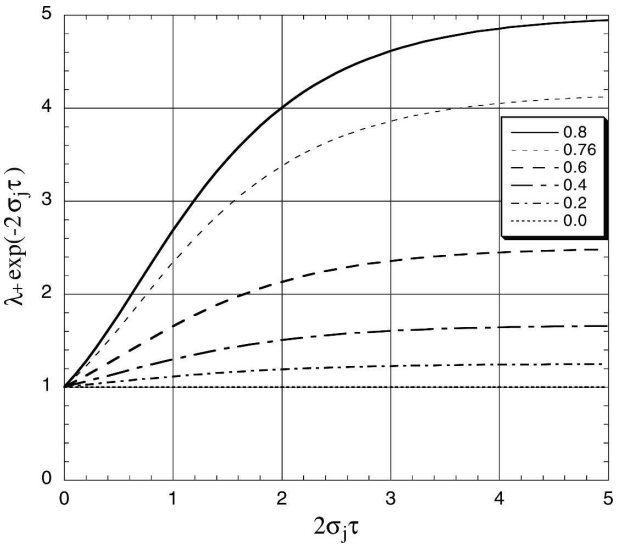

FIG. 6. Plot of $\lambda_+ \exp(-2\sigma_j\tau)$ for different values of γ^2 (=0, 0.2, 0.4, 0.6, 0.76, 0.8) over the range of $0 \leq 2\sigma_j\tau \leq 5$. Here λ_+ is the largest eigenvalue in the subspace spanned by pair of growing and decaying modes (represented by the jth and j'th modes with $j = -j' > 0$), and $\sigma_j > 0$ is the growth rate of the (jth) growing mode.

For case 2, we have $\sigma_1 = \sigma_{\max} = 0.20$. As discussed in section 3b, the nonmodal growth is dominated by the fastest growing mode when $\tau > 3.5$. In this case, since $\gamma^2 = 0.76$ and $(1 - \gamma^2)^{-1} = 4.16$ for the paired fastest growing and decaying modes, the scaled growth (shown by the dashed curve in Fig. 2) can be enhanced up to 4.16 times by including the fastest decaying mode. When $\tau < 3.5$, however, the nonmodal growth is produced mainly by paired propagating modes, and the scaled growth is shown by the dashed curve in Fig. 2. The scaled growth produced by the paired fastest growing and decaying modes (with $\gamma^2 = 0.76$) is shown by the dotted curve in Fig. 6. This curve is lower than the dashed curve in Fig. 2 only when $\tau < 1.25$ ($2\sigma_1\tau < 0.5$). Thus, for case 2, the scaled growth can be enhanced by adding the fastest decaying mode for $\tau > 1.25$. When $\tau \leq 0.7$ ($2\sigma_1\tau < 0.28$), the effect of the fastest decaying mode becomes insignificant and the paired fastest propagating modes dominate the leading singular perturbation (as discussed in sections 3b and 4a).

c. Paired stationary and linearly growing modes

As shown in section 3c of Part I, when $\mathrm{Ri}_{\mathrm{nc}}(k) \equiv 1 - (n_c l/2)^2 \to \mathrm{Ri} < 1$ (as l changes) or $\mathrm{Ri} \to \mathrm{Ri}_{\mathrm{nc}}$ (as Ri changes), $\sigma_+(n_c) \to 0$ and the associated pair of modes degenerates into a pair of stationary and linearly grow-

ing modes. Denote by $\mathbf{A}_j(t)$ the 2×2 submatrix of $\mathbf{A}(t)$ associated with the subspace spanned by this pair of stationary and linearly growing modes for which $j = 2(n-1)\mathrm{sgn}(m) + m = \pm(2n_c + 1)$. By using (3.7)–(3.8) of Part I, one can show that $\mathbf{A}_j(t)$ has the following form:

$$\mathbf{A}_j(t) = X_j \begin{pmatrix} 0 & 0 \\ 0 & 1 \end{pmatrix} + Z_j \begin{pmatrix} 1 & t \\ t & t^2 \end{pmatrix}, \tag{4.9}$$

where X_j and Z_j are defined as in (4.2) but with $\mathrm{Ri} = \mathrm{Ri}_{nc}$, $n = n_c$ and $\beta_j^2 = 1$ since $|\omega_j| = |\sigma_j| = 0$. In this case, the eigenvalue problem in (2.5) reduces to (4.3) but with $\mathbf{A}_j(\tau)$ and $\mathbf{A}_j(0)$ given by (4.9). As shown in appendix C, the reduced eigenvalue problem has two eigenvalues given by $\lambda_\pm = q_j \pm (q_j^2 - 1)^{1/2}$ as in (4.4) but with

$$q_j = 1 + \rho^2\tau^2/2, \tag{4.10}$$

where $\rho^2 = Z_j/X_j$. Note that $\lambda_+ \to \rho^2\tau^2 \to \infty$ as $\tau \to \infty$. In this limit, the energy growth λ_+ (in the subspace spanned by the paired stationary and linearly growing modes) is produced entirely by the linearly growing mode [see (3.8) of Part I and appendix C].

The result in (4.10) can be also derived from (4.5) or (4.8) in the limit of $|\omega_j| = |\sigma_j| \to 0$. Note that $\gamma = (X_j - Y_j)/(X_j + Y_j) \to -1 + 2|\sigma_j|^2 X_j/Z_j + \mathrm{O}(|\sigma_j|^4)$ as $|\sigma_j| \to 0$. Using this result and the Taylor expansion of $\cos(2\omega_j\tau)$ with $\omega_j^2 = -\sigma_j^2$ (>0), one can verify that (4.5) degenerates into (4.10) in the limit of $|\omega_j| \to 0$. Similarly, (4.8) degenerates into (4.10) in the limit of $|\sigma_j| \to 0$.

5. Nonmodal growth patterns and classification

In this section, the analytical results obtained in the previous section will be used to examine the distributions of the maximum nonmodal growths (produced by paired modes) in the parameter space of (l, Ri) for different optimization times in comparison with the numerical results obtained in section 3. The nonmodal growths will be classified into four types based on the analytical results and their comparisons with the numerical results.

As we have seen in the previous section, by using (4.4)–(4.6), (4.8), and (4.10), we can obtain λ_+ precisely in any subspace spanned by two paired modes. Denote by λ_{j+} the maximum nonmodal growth in the jth subspace (spanned by the jth paired modes). Denote by $\max(\lambda_{j+})_N = \max\{\lambda_{j+} \mid j = 1, 2, \ldots, 2N\}$ the maximum among all λ_{j+} for $j = 1, 2, \ldots, 2N$. Since $j = 2(n-1)\mathrm{sgn}(m) + m$ and m ($=\pm1, \pm2$), $j = 2N$ is associated with $n = N$ where n is the vertical mode number. In section 3, the nonmodal growths are computed in the truncated space (with $n \le N = 15$ or, equivalently, $|j| \le 2N = 30$). The computed nonmodal growth is scaled by $\exp(2\mathrm{Re}\sigma_1\tau)$ and plotted in Fig. 1 for $\tau = 0.5$. To compare the results obtained in section 4 with those in section 3, $\max(\lambda_{j+})_N$ is computed also with $N = 15$ and scaled by $\exp(2\mathrm{Re}\sigma_1\tau)$, as shown in Fig. 7a for $\tau = 0.5$.

The scaled nonmodal growth in Fig. 7a has nearly the same pattern as that in Fig. 1 except for the upper-left and lower-left corner regions. Over the broad region of $l > 0.5$, the scaled nonmodal growth in Fig. 7a is very close to (only slightly smaller than) that in Fig. 1 and $\max(\lambda_{j+})_N$ is given by λ_{2+}. This means that the maximum nonmodal growth is produced dominantly by the paired fastest propagating modes (with $j = 2$). When l is smaller than 0.5 and decreases continuously (toward zero), $\max(\lambda_{j+})_N$ is given by λ_{4+}, λ_{6+}, λ_{8+}, ... consecutively. In this case, the scaled nonmodal growth in Fig. 7a is still quite close to that in Fig. 1 in the region of $1.2 > \mathrm{Ri} > 0.8$, so the maximum nonmodal growth is produced mainly by the jth paired fast propagating modes with $j = 4, 6, 8, \ldots$ consecutively as l decreases (roughly from 0.5 to 0.1). In the upper-left corner region ($\mathrm{Ri} > 1.2$ and $l < 0.5$) and lower-left corner region ($\mathrm{Ri} < 0.8$ and $l < 0.5$), the scaled nonmodal growth in Fig. 7a is significantly smaller than that in Fig. 1. In this case, the jth paired fast propagating modes (with $j = 4, 6, 8, \ldots$ consecutively as l decreases from 0.5 toward zero) explain only a part of the nonmodal growth in Fig. 1.

When the optimization time is increased from $\tau = 0.5$ to 1.0, the scaled nonmodal growth is increased significantly in two regions, as shown by Fig. 7b in comparison with Fig. 7a. One region is in the vicinity of the curved boundary of the unstable region below $\mathrm{Ri} = 1$, while the other region is marked by the semicircle counter (of 2.0) centered at $l = 0.1$ and $\mathrm{Ri} = 1.2$. In the upper part ($1 > \mathrm{Ri} > 0.7$) of the curved region, $\max(\lambda_{j+})_N$ is given by λ_{4+}, λ_{6+}, λ_{8+}, ... as l becomes smaller than 2.0, 1.0, 0.5, ..., respectively. In the lower part ($\mathrm{Ri} < 0.7$) of the curved region, $\max(\lambda_{j+})_N$ is given by λ_{1+}. Note that λ_{1+} is the maximum nonmodal growth produced by the paired slowest propagating modes (or by the paired fastest growing and decaying modes) when the parameter point (l, Ri) is outside (or inside) the unstable region. When the parameter point (l, Ri) is outside the unstable region, the nonmodal growth in Fig. 7b matches closely the maximum nonmodal growth computed in the truncated space with $n \le N = 15$ (not shown). Inside the unstable region, the scaled nonmodal growth in Fig. 7b is larger than that (not shown) computed in the truncated space with $n \le N = 15$ (not shown) in which the decaying modes are excluded.

When the optimization time is increased further to $\tau = 5.0$, the scaled nonmodal growth is increased

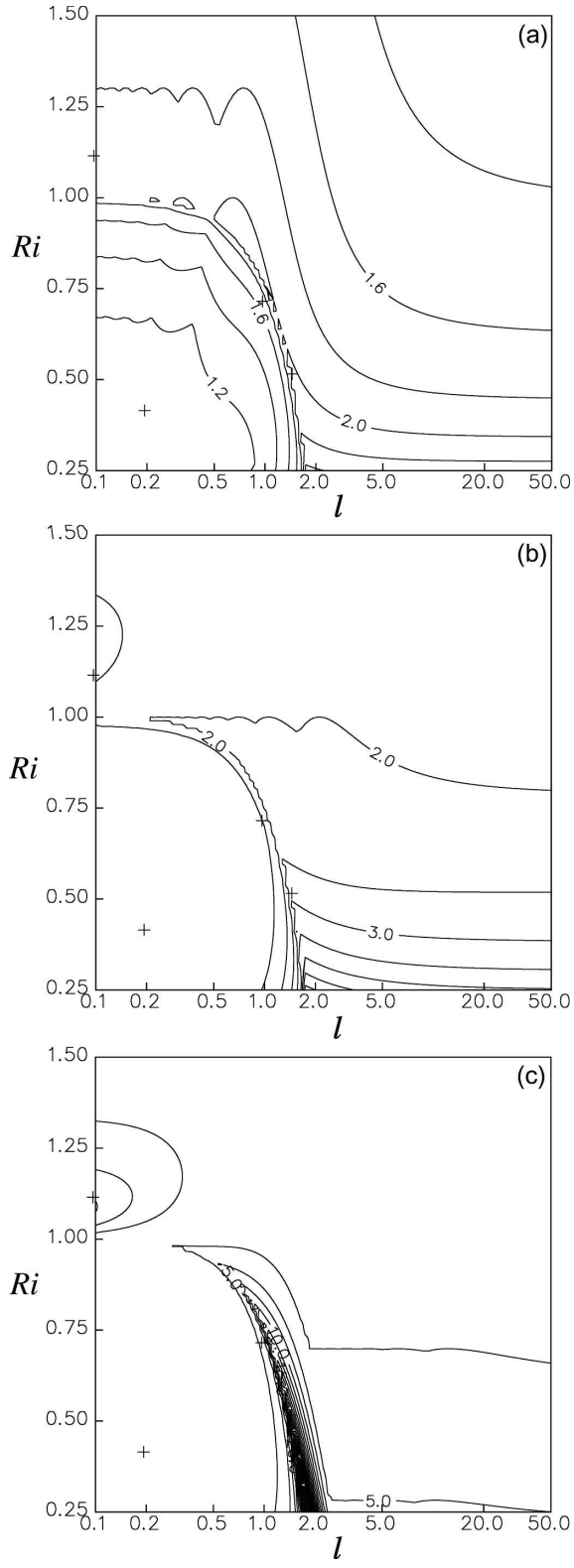

FIG. 7. As in Fig. 1 but for contours of $\max(\lambda_{j+})_N \exp(-2\mathrm{Re}\sigma_1\tau)$ with $N = 15$ plotted in the parameter space of (l, Ri) for $\tau =$ (a) 0.5, (b) 1.0, and (c) 5.0. The contour intervals are 0.2 in (a), 0.5 in (b), and 2.5 in (c).

sharply in the banana-shaped region along the boundary of the unstable region (see Fig. 7c). The scaled nonmodal growth is also increased by three times in the semicircle region, while the center of the semicircle region is shifted slightly down to Ri = 1.1 (Fig. 7c). In these two regions and outside the unstable region, the scaled growth is very close to that (not shown) computed in the truncated space (with $n \le N = 15$). In this case, $\max(\lambda_{j+})_N$ is given by λ_{1+}, so the maximum nonmodal growth is produced almost solely by the paired slowest propagating modes. Inside the unstable region, $\max(\lambda_{j+})_N$ is also given by λ_{1+}, but λ_{1+} is produced by the paired fastest growing and decaying modes. In this case, the scaled growth in Fig, 7c is larger than that (not shown) computed in the truncated space in which the decaying modes are excluded.

Note that the semicircle region (marked by the contour of 2.5) in Fig. 7c largely coincides with the semicircle region of $\gamma > 0.7$ centered at $l = 0.1$ (with $n = 1$) and Ri = 1.1 in Fig. 5a. In this region, we have $\gamma > 0.7$ and thus $X_j/Y_j = (1 + \gamma)/(1 - \gamma) > 9.0$ for j $= \pm 1$. In this case, since $X_j > Y_j$, the nonmodal growth of the total perturbation energy (produced by the paired slowest propagating modes with j $= \pm 1$) is characterized by the increase of the cross-band kinetic energy $\{K_2\}$ that excessively offsets the decrease of $\{K_v + P_b\}$. In particular, as shown in section 4a, this type of nonmodal growth reaches the maximum of $\lambda_+ = X_j/Y_j$, as $\tau = \pi/(2\omega_j)$. In this case, $\{K_2\}$ increases from 0 to $4X_j$ and $\{K_v + P_b\}$ decreases from $4Y_j$ to 0 as t increases from 0 to $\tau = \pi/(2\omega_j)$. This type of nonmodal growth requires $X_j > Y_j$ and is classified as PP1 for paired propagating modes. According to (B.5) and the related discussion in subsection c of appendix B, $X_j/Y_j \to \infty$ and $\gamma \to 1$ as (nl, Ri) $\to (0, 1_+)$ outside the unstable region, so the PP1 growth can become unboundedly large only when (nl, Ri) $\to (0, 1_+)$ outside the left boundary of Fig. 5a.

The banana-shaped region in Fig. 7c largely coincides with the trough region of $\gamma < -0.7$ (with $n = 1$) in Fig. 5a. In this region, we have $-1 \le \gamma < -0.8$ and thus $0 \le X_j/Y_j = (1 + \gamma)/(1 - \gamma) < 0.11$ for $j = \pm 1$. Here $\gamma = -1$ corresponds to $X_j/Y_j = 0$ for j $= \pm 1$ while the latter corresponds to $\sigma_1 = 0$ for parameter points along the boundary of the unstable region (see Fig. 1a of Part I) or, equivalently, along the ridge of the banana-shaped region in Fig. 7c. Immediately outside the unstable region on the long-wavelength side from the ridge of the banana-shaped region in Fig. 7c, the nonmodal growth of the total perturbation energy (produced by the paired slowest propagating modes with j $= \pm 1$) is characterized by the increase of $\{K_v + P_b\}$ that excessively offsets the decrease of $\{K_2\}$. This type of nonmodal

growth requires $X_j < Y_j$ and is classified as PP2 for paired propagating modes. The PP2 nonmodal growth reaches the maximum of $\lambda_+ = Y_j/X_j$ as $\tau = \pi/(2\omega_j)$. Clearly, the physical mechanism for the PP2 nonmodal growth is opposite to that for PP1, although both types of growths are produced by paired propagating modes.

Immediately inside the unstable region on the short-wavelength side from the ridge of the banana-shaped region in Fig. 7c, the nonmodal growth (produced by the paired fastest growing and decaying modes) is much larger than the fastest modal growth and the scaled nonmodal growth is much larger than one. In this region, $-1 < \gamma < -0.8$ and $\infty > (1 - \gamma^2)^{-1} > 2.7$, so the scaled nonmodal growth can be very large and very close to its asymptotic limit $(1 - \gamma^2)^{-1}$ as τ is sufficiently large (see Fig. 6). In this case, as explained in section 4b, since $\gamma < 0$ and thus $X_j < Y_j$, the nonmodal growth is caused by the reduction of $\{K_v + P_b\}$ that excessively offsets the increase of $\{K_2\}$ at the initial time due to the inclusion of the decaying mode. This type of nonmodal growth requires $X_j < Y_j$ and is classified as GD2 for paired growing and decaying modes.

There is another semicircle region in Fig. 7c that largely coincides with the semicircle region of $\gamma > 0.7$ centered at $l = 0.1$ (with $n = 1$) and Ri = 0.9 in Fig. 5a. In this region, the scaled nonmodal growth has a local maximum at $l = 0.1$ and Ri = 0.9 but this maximum is below 2.5 and thus is not shown by the contours (every 2.5) in Fig. 7c. Since $\gamma > 0$ and thus $X_j > Y_j$ in this region, the nonmodal growth is caused by the reduction of $\{K_2\}$ that excessively offsets the increase of $\{K_v + P_b\}$ at the initial time due to the inclusion of the decaying mode. This type of nonmodal growth requires $X_j > Y_j$ and is classified as GD1 for paired growing and decaying modes. According to (B.5) and the related discussion in subsection c of appendix B, $X_j/Y_j \to \infty$ and $\gamma \to 1$ as $(nl, \text{Ri}) \to (0, 1_-)$ inside the unstable region, so the GD1 growth can become unboundedly larger than the fastest modal growth only when $(nl, \text{Ri}) \to (0, 1_-)$ outside the left boundary of Fig. 5a.

6. Conclusions

In this paper, the total perturbation energy defined in Part I is used to measure the nonmodal growths of symmetric perturbations, and the complete set of normal modes presented in Part I is truncated and used to construct nonmodal perturbations. For a given optimization time τ, the maximum nonmodal growth is given by the largest eigenvalue of the eigenvalue problem formulated with the total perturbation energy norm. To prevent the eigenvalue problem from becoming ill conditioned (as τ becomes large), the decaying modes are excluded from the truncated normal mode space (for the computations presented in section 3 only). The largest eigenvalues are computed as functions of τ for different settings of horizontal wavelength l and Richardson number Ri. The computed eigenvalues and associated singular vectors are examined in terms of optimal combinations of different normal modes for the four cases of different settings of (l, Ri) considered in Part I. The results are summarized as follows:

1) The maximum nonmodal energy growth is larger than the energy growth of the fastest growing mode if the parameter point (l, Ri) is within the unstable region [determined by $\text{Ri} < 1 - (l/2)^2$]. If the parameter point (l, Ri) is outside the unstable region, then there is no growing mode but nonmodal perturbations can grow owing to optimal combinations of different normal modes.
2) When the optimization time is very short (compared with the inverse Coriolis parameter), the maximum nonmodal growth is produced mainly by the paired fastest propagating modes. When the optimization time is not short and the parameter point (l, Ri) is near the boundary outside the unstable region (see case 3 in section 3), the maximum nonmodal growth is produced almost solely by the paired slowest propagating modes and the growth can be very large for a wide range of optimization time.
3) When the parameter point (l, Ri) is near the boundary inside the unstable region (see case 2 in section 3), the paired slowest propagating modes can contribute significantly to the energy growth before the fastest growing mode becomes the dominant component. The fastest growing mode becomes the dominate component as the optimization time is sufficiently large.

Note that the normal modes are nonorthogonal (measured by the inner product associated with the total perturbation energy norm). This basic fact explains the above result 1. Also, as shown in section 5 of Part I, the streamfunction component modes are orthogonal between different pairs and initially parallel within each pair in the streamfunction subspace. This basic property can partially explain why the maximum nonmodal growths of symmetric perturbations can be produced dominantly by paired modes, as summarized in the above results 2 and 3. However, since the decaying modes are excluded from the truncated normal mode space, their effect on the nonmodal growths is not reflected by the above result 3. The effect of the decaying modes can be significant as shown by the analysis of paired growing and decaying modes in section 4b.

The maximum nonmodal growths produced by paired modes are solved analytically in section 4 and classified into four types in section 5. The analytical solutions compare well with the numerical results obtained in the truncated normal mode space. The simplicity of the analytical solutions reveals the basic mechanisms for the nonmodal energy growths of symmetric perturbations. Note that two paired modes have opposite polarization relationships. In particular, the two modes have the same cross-band velocity fields but opposite along-band velocity and buoyancy fields at the initial time, so they have the same initial cross-band kinetic energy X_j and the same initial along-band kinetic and buoyancy energy Y_j [see (4.2)]. With these understandings, the basic mechanisms for the four types of nonmodal energy growths and associated nonmodal structures can be highlighted as follows:

(i) If $X_j > Y_j$ (or $X_j < Y_j$) for a pair of propagating modes, then the two modes can be combined to offset each other's cross-band velocity (or along-band velocity and buoyancy) and thus to minimize the total perturbation energy to $4Y_j$ (or $4X_j$) at the initial time. As the two modes propagate toward each other through one-half of the wavelength, their associated cross-band velocity (or along-band velocity and buoyancy) fields become exactly in phase, so the total perturbation energy is increased to $4X_j$ (or $4Y_j$) and the nonmodal growth reaches the maximum value of X_j/Y_j (or Y_j/X_j). The nonmodal growth produced by paired propagating modes is classified as PP1 type if $X_j > Y_j$ or as PP2 type if $X_j < Y_j$. The PP1 growth is characterized by the increase of the cross-band kinetic energy that excessively offsets the decrease of the along-band kinetic and buoyancy energy. The situation is opposite for the PP2 growth. Thus, the PP1 and PP2 nonmodal solutions are simply standing waves. Each component field of the standing wave has the same pattern as the corresponding modal component field (see, e.g., Figs. 3 and 4 of Part I) but the patterns oscillate in place (rather than propagate) and the oscillation of X_j is opposite to that of Y_j.

(ii) For a pair of growing and decaying modes, the two modes can be also combined to reduce the cross-band kinetic energy if $X_j > Y_j$ (or the along-band kinetic and buoyancy energy if $X_j < Y_j$) at the initial time and thus to enhance the growth of the total perturbation energy at the optimization time (see section 4b and Fig. 6). In this case, the inclusion of the decaying mode reduces the total energy more at the initial time than at the optimization time, so the nonmodal energy growth can be enhanced by a factor up to $(X_j + Y_j)^2/(4X_jY_j)$ as the optimization time approaches infinity. The nonmodal growth produced by paired growing and decaying modes is classified as GD1 type if $X_j > Y_j$ or as GD2 type if $X_j < Y_j$. Each component field of the GD1 or GD2 nonmodal solution has the same pattern as the corresponding modal component field (see, e.g., Fig. 2 of Part I). The nonmodal solution approaches asymptotically to the fastest growing mode.

The nonmodal growths produced by paired fast propagating modes all belong to the PP2 type (see Figs. 5b and 7a). When the optimization time is sufficiently short, the maximum nonmodal growth is produced mainly by the paired fastest propagating modes and thus is the PP2 type. When the optimization time is large, the maximum nonmodal growth is produced mainly by the paired slowest propagating modes (or fastest growing and decaying modes) if the parameter point (l, Ri) is outside (or inside) the unstable region. Outside the unstable region, the maximum nonmodal growth is the PP1 type on the short-wavelength side (see Figs. 5a and 7c, and the related discussions in section 5 and section c of appendix B), but changes to the PP2 type on the long-wavelength side and becomes very large as the parameter point (nl, Ri) approaches the boundary of the unstable region (see Figs. 5a and 7c). Inside the unstable region, the maximum nonmodal growth is the GD1 type on the short-wavelength side (see Figs. 5a and 7c, and related discussions), but changes to the GD2 type on the long-wavelength side as the parameter point (nl, Ri) approaches the boundary of the unstable region.

Although the GD1 or GD2 nonmodal growth is larger than the energy growth produced by the fastest growing mode, the nonmodal growth rate always approaches the constant modal growth rate as the optimization time increases. Unless the parameter point (nl, Ri) is immediately inside the unstable region [see (B.5), Figs. 5a and 7c], the transient nonmodal growth rate is not much larger than the modal growth rate and the growth rate approaches the modal growth rate within two e-folding time periods ($2\sigma_j\tau \leq 4$ as shown in Fig. 6). Because of this, the GD1 or GD2 nonmodal growth (if it occurs) will play essentially the same role as the modal growth in generating some of the observed symmetric perturbations (Bennetts and Sharp 1982; Parsons and Hobbs 1983; Dixon et al. 2002).

The PP1 nonmodal growth produced by paired slowest propagating modes can be very large only when the parameter point (nl, Ri) is very close to $(0, 1_+)$ [see (B.5), Figs. 5a and 7c, and the related discussions in

section 5 and appendix B]. As this type of nonmodal growth is characterized by the increase of the cross-band kinetic energy (from 0 to $4X_j$), it may generate strong cross-band vertical circulation over a wide range of optimization time. The PP2 nonmodal growth produced by paired fastest propagating modes is not significant because the growth is small (between 1 and 2.4 for $\tau = 0.5$ as shown in Fig. 7a) and lasts only for a short time ($\tau < 1$). The PP2 nonmodal energy growth produced by paired slowest propagating modes (with $l > 1$), however, can be very large and last for a long time, especially when the parameter point (l, Ri) is near the unstable region. This type of nonmodal growth is characterized by the increase of the along-band kinetic and buoyancy energy (from 0 to $4Y_j$).

Note that the vertical displacement (obtained by the time-integration of the vertical component of the cross-band velocity) is proportional to the along-band velocity and buoyancy, so the PP2 type of nonmodal growth may provide a large vertical lift in the lower troposphere to trigger or enhance moist convection. The energy norm used in this paper, however, does not directly measure the vertical displacement. Note also that the classic inertial gravity wave modes in nonsheared basic flows do not produce the nonmodal growths examined in this paper [see (B.11) and the related discussion in appendix B]. To study the nonmodal growth of the vertical displacement produced by inertial gravity waves in sheared basic flows (including the propagating modes studied in this paper) in terms of triggering or enhancing moist convection, a new metric needs to be introduced. This problem is under our investigation.

Moist convection and convective storms can be triggered or enhanced by propagating inertial gravity waves in many different ways in the atmosphere. The related wave dynamics often appear to be approximately linear and may become more or less nonmodal as they propagate into other preexisting perturbations, such as mesoscale convective systems (Uccellini 1975; Koch et al. 1988) or moisture bands (Fovell et al. 2004). The propagating inertial gravity waves and pre-existing perturbations may produce significant nonmodal growths in a sheared environmental flow if their structures become increasingly in-phase in the component fields that dominate the nonmodal growth [such as the (u, v) components for the PP1 nonmodal growth or (v, b) components for the PP2 nonmodal growth] owing to a similar mechanism as described above for paired propagating modes. In the real atmosphere, exactly paired modes may rarely occur, but quasi-paired modes may occur and perhaps produce suboptimal nonmodal growths. For example, the slowly propagating mode (with $l = 1.5$ and Ri = 0.5 for case 3) in Fig. 4 of Part I could be quasi-paired with a growing mode of slightly shorter wavelength (such as $l = 1.2$ for the same Ri = 0.5). A packet of the former is a slowly propagating inertial gravity wave train, and a packet of the latter may resemble a mesoscale convective system. When the former propagates into the latter, a nonmodal growth may be produced locally (measured by a localized norm) if their structures become increasingly in-phase in the dominant component fields as speculated above. Because quasi-paired modes are more likely to occur than exactly paired modes, their produced local nonmodal growths deserve further studies in connection with symmetric and nearly symmetric perturbations observed in the real atmosphere, and this may include the scenario envisioned in the introduction (paragraph 2) of Part I.

Acknowledgments. The authors are thankful to Dr. Robert Davies-Jones and the anonymous reviewers for their comments and suggestions that improved the presentation of the results. The work was supported by the NSF Grant ATM-9983077 to the University of Oklahoma and by the National Natural Science Foundation Grant 40205010 and KZCX2-208 of Chinese Academy of Sciences.

APPENDIX A

Solution of (4.3) for Paired Propagating Modes

According to (4.1), we have

$$\mathbf{A}_j(0) = p_j \begin{pmatrix} 1 & \gamma \\ \gamma & 1 \end{pmatrix} \quad \text{and}$$

$$\mathbf{A}_j(\tau) = p_j \begin{pmatrix} 1 & \gamma \exp(i2\omega_j\tau) \\ \gamma \exp(-i2\omega_j\tau) & 1 \end{pmatrix}, \quad \text{(A.1)}$$

where $p_j = X_j + Y_j$ and $\gamma = (X_j - Y_j)/p_j$. Note from (4.2) that $X_j > 0$ and $Y_j > 0$, so $-1 < \gamma < 1$. It is also easy to verify that

$$\mathbf{A}_j(0) = p_j \mathbf{R}\mathbf{\Lambda}\mathbf{\Lambda}\mathbf{R}, \quad \text{(A.2)}$$

where $\mathbf{R} = \mathbf{R}^{\mathrm{T}} = \mathbf{R}^{-1}$ is given by

$$\mathbf{R} = \frac{1}{\sqrt{2}} \begin{pmatrix} 1 & 1 \\ 1 & -1 \end{pmatrix} \quad \text{and} \quad \mathbf{\Lambda}\mathbf{\Lambda} = \begin{pmatrix} 1+\gamma & 0 \\ 0 & 1-\gamma \end{pmatrix}. \quad \text{(A.3)}$$

Substituting (A.3) into (4.3) gives $[\mathbf{A}_j(\tau) - \lambda p_j \mathbf{R}\mathbf{\Lambda}\mathbf{\Lambda}\mathbf{R}]\mathbf{c}_j = 0$ or, equivalently,

$$(\mathbf{B}_j - \lambda \mathbf{I})\mathbf{d}_j = 0, \quad \text{(A.4)}$$

where $\mathbf{I}$ is the unit matrix,

$$\mathbf{B}_j = p_j^{-1}\mathbf{\Lambda}^{-1}\mathbf{R}\mathbf{A}_j(\tau)\mathbf{R}\mathbf{\Lambda}^{-1} = (1+\gamma)^{-1}\begin{pmatrix} 1+\gamma\cos(2\omega_j\tau) & -i\gamma\Omega\sin(2\omega_j\tau) \\ i\gamma\Omega\sin(2\omega_j\tau) & [1-\gamma\cos(2\omega_j\tau)]\Omega^2 \end{pmatrix}, \tag{A.5}$$

$$\mathbf{d}_j = \mathbf{\Lambda}\mathbf{R}\mathbf{c}_j \quad \text{and}$$

$$\Omega^2 = (1+\gamma)/(1-\gamma) = X_j/Y_j > 0$$

[see (A.1) and (4.2)].

As the eigenvalue problem in (4.3) is converted into (A.4), the eigenvalues are the two roots of $\det(\mathbf{B}_j - \lambda\mathbf{I}) = \lambda^2 - 2\lambda q_j + 1 = 0$, where (A.5) is used and

$$q_j = [1-\gamma^2\cos(2\omega_j\tau)]/(1-\gamma^2). \tag{A.6}$$

The two eigenvalues are thus given by

$$\lambda_\pm = q_j \pm (q_j^2 - 1)^{1/2}. \tag{A.7}$$

As shown by (A.6), q_j is a periodic function of τ, and so are the eigenvalues in (A.7). When $\tau = n\pi/\omega_j$ (for any integer $n \geq 0$), we have $\cos(2\omega_j\tau) = 1$, $q_j = 1$ and $\lambda_\pm = 1$. When $\tau = (n+1/2)\pi/\omega_j$, we have $\cos(2\omega_j\tau) = -1$, $q_j = (1+\gamma^2)/(1-\gamma^2)$ and $\lambda_\pm = (1 \pm |\gamma|)^2/(1-\gamma^2)$. Note from (4.2) that $X_j > 0$ and $Y_j > 0$, so $0 < |\gamma| = |X_j - Y_j|/(X_j + Y_j) = <1$ as long as $X_j \neq Y_j$. Thus, $\lambda_+ = (1+|\gamma|)/(1-|\gamma|) = \max(\Omega^2, \Omega^{-2}) > 1 > \min(\Omega^2, \Omega^{-2}) = (1-|\gamma|)/(1+|\gamma|) = \lambda_-$ when $\tau = (n+1/2)\pi/\omega_j$ and $X_j \neq Y_j$ ($\Omega^2 \neq 1$). If $X_j = Y_j$, then $\gamma = 0$, $\Omega^2 = 1$, $q_j = 1$, and $\lambda_\pm = 1$ for any τ. In this case, $\mathbf{A}_j(0)$ and $\mathbf{A}_j(\tau)$ reduce to $p_j\mathbf{I}$ in (A.1) and the eigenvalue problem in (4.3) becomes trivial.

When $\tau = n\pi/\omega_j$, $\mathbf{B}_j$ in (A.5) reduce to $\mathbf{I}$, so the two eigenvalues collapse into $\lambda_\pm = 1$. This is consistent with the above analysis of (A.6)–(A.7). In this case, the eigenvalue problem becomes trivial and the eigenvectors become arbitrary. When $\tau = (n+1/2)\pi/\omega_j$ and thus $\sin(2\omega_j\tau) = 0$, $\mathbf{B}_j$ in (A.5) becomes a diagonal matrix; that is, $\mathrm{diag}(\Omega^{-2}, \Omega^2)$. This result is also consistent with the above analysis of (A.6)–(A.7). In this case, if $X_j > Y_j$, then the maximum nonmodal growth is given by $\lambda_+ = \Omega^2$ ($= X_j/Y_j > 1$) in the jth subspace and the associated eigenvector is given by $\mathbf{d}_j = (0, 1)^{\mathrm{T}}$ for the eigenvalue problem in (A.4) or, equivalently, by $\mathbf{c}_j = \mathbf{R}\mathbf{\Lambda}^{-1}\mathbf{d}_j \propto (1, -1)^{\mathrm{T}}$ for the eigenvalue problem in (4.3). If $X_j < Y_j$, then the maximum nonmodal growth is given by $\lambda_+ = \Omega^{-2}$ ($= Y_j/X_j > 1$) and the associated eigenvector is given by $\mathbf{d}_j = (1, 0)^{\mathrm{T}}$ for the eigenvalue problem in (A.4) or, equivalently, by $\mathbf{c}_j = \mathbf{R}\mathbf{\Lambda}^{-1}\mathbf{d}_j \propto (1, 1)^{\mathrm{T}}$ for the eigenvalue problem in (4.3).

APPENDIX B

Asymptotic Behaviors of X_j/Y_j and γ

a. Asymptotic behaviors of X_j/Y_j and γ as $\mu \to 0$

Note that $\mu = k/(n\pi) = 2/(nl)$, so $\mu \to 0$ as $nl \to \infty$. In this large-scale limit, we have

$$\sigma_\pm^2 \to -1 \pm \mu \to -1 \quad \text{and} \quad \beta_\pm \to \pm\mu^{-1} \to \pm\infty. \quad \text{as} \quad \mu \to 0, \tag{B.1}$$

where $\sigma_\pm^2$ are the roots of (3.3) of Part I and $\beta_\pm \equiv (1+\sigma_\pm^2)^{-1}$. Substituting (B.1) into (4.2b)/(4.2a), and (4.6) gives

$$Y_j/X_j \to 1 + \mathrm{Ri}^{-1} \quad \text{and} \quad \gamma \to -1/(1+2\mathrm{Ri}) \quad \text{as} \quad \mu \to 0. \tag{B.2}$$

b. Asymptotic behaviors of X_j/Y_j and γ as $\mu \to \infty$

In the small-scale limit ($nl \to 0$), we have

$$\sigma_\pm^2 \to s_\pm^2 \equiv -(1+r^{-2})/2 \pm [(1+r^{-2})^2/4 + (\mathrm{Ri}^{-1} - 1)/r^2]^{1/2} \quad \text{as} \quad \mu \to \infty, \tag{B.3}$$

where $a^2 = r^2\mathrm{Ri}$ is used [see (2.4) of Part I]. Here, $\pm s_+$ correspond to paired slowly propagating modes (if $s_+^2 < 0$) or paired growing and decaying modes (if $s_+^2 > 0$) with $m = \pm 1$, while $\pm s_-$ correspond to paired fast propagating modes with $m = \pm 2$. As explained in (2.1), m ($= \pm 1, \pm 2$) is the root number for the four roots ($\pm\sigma_+, \pm\sigma_-$). The small-scale limit of (4.2b)/(4.2a) gives

$$Y_j/X_j \to T_j \equiv [1 + \mathrm{Ri} + \beta_j^2(1+\mathrm{Ri}^{-1}) - 4\beta_j]/[(r^2\mathrm{Ri} + \beta_j^2)|s_j|^2] \quad \text{as} \quad \mu \to \infty, \tag{B.4}$$

where $\beta_j = (1+s_j^2)^{-1}$, $s_j^2 = s_+^2$ for $j = \pm[2(n-1)+1]$ with $m = \pm 1$, and $s_j^2 = s_-^2$ for $j = \pm[2(n-1)+2]$ with $m = \pm 2$. As shown by (B.3) and (B.4), T_j is a function of (Ri, r^2) only. Since r^2 is small ($=0.02$ as given in Part I), T_j depends mainly on Ri. For $s_j^2 = s_-^2$ (paired fast propagating modes), T_j is a monotonic function of Ri and decreases smoothly from 4.6 to 0.84 as Ri increases from 0.25 to 1.5 (with $r^2 = 0.02$). For $s_j^2 = s_+^2$ (paired slowly propagating modes or paired growing and decaying modes), T_j decreases from 2.6 (or 0.33) toward 0 as Ri increases from 0.25 (or decreases from 1.5) toward 1.0 (with $r^2 = 0.02$) in the unstable (or stable) region.

By using (B.4), one can verify that for $j = \pm[2(n-1)+1]$ with $m = \pm 1$ (i.e., $s_j^2 = s_+^2$)

$$Y_j/X_j \to T_j \to \varepsilon(1 + r^2 + r^4 + r^6)/(1 + r^2)^3 \to 0 \quad \text{and thus}$$
$$\gamma \to 1 \quad \text{as} \quad \mu \to \infty \quad \text{and then} \quad \text{Ri} - 1 = \pm\varepsilon \to 0, \tag{B.5}$$

where $1 \gg \varepsilon > 0$. This limit is obtained (for $s_j^2 = s_+^2$) by taking $\mu \to \infty$ first and then taking Ri $\to 1$ from $1 + \varepsilon > 1$ (or $1 - \varepsilon < 1$) in the stable (or unstable) region. As shown in the next subsection, if Ri $\to 1$ first, then Y_j/X_j will have a different value (=2) at Ri = 1.

c. Asymptotic behaviors of X_j/Y_j and γ as Ri $\to 1$

When Ri $\to 1$, Eq. (3.3) of Part I reduces to

$$(1 + \mu^2 a^2)(1 + \sigma_j^2)^2 + \mu^2(1 - a^2)(1 + \sigma_j^2) + \mu^2 = 0. \tag{B.6}$$

Multiplying β_j to (B.6) gives

$$(1 - |\omega_j|^2)[1 + (a^2 + \beta_j^2)\mu^2] + (1 - a^2)\mu^2 - 2\beta_j\mu^2 = 0, \tag{B.7}$$

where $\beta_j^{-1} = 1 + \sigma_j^2 = 1 - |\omega_j|^2$ is used [see (3.1) of Part I]. Multiplying $(n\pi)^2/2$ to (B.7) gives

$$2X_j + (1 - a^2)k^2/2 - \beta_j k^2 = 2|\omega_j|^2 X_j, \tag{B.8}$$

where $X_j = [(n\pi)^2 + (a^2 + \beta_j^2)k^2]/4$ is the same as in (4.2a). Note that the left-hand side of (B.8) is the same as $|\omega_j|^2 Y_j = Z_j$ in (4.2c) for Ri = 1, so (B.8) gives

$$Y_j/X_j = 2 \quad \text{and} \quad \gamma = -1/3 \quad \text{as} \quad \text{Ri} = 1 \text{ for any } \mu. \tag{B.9}$$

This result is valid for all paired propagating modes, as we can see from Figs. 5a,b.

The results in (B.5) and (B.9) imply that the contours of γ collapse as (nl, Ri) $\to$ (0, 1) in the parameter space outside the left boundary of Fig. 5a. If $l \to 0$ and $\varepsilon =$ Ri $- 1 \to 0$ simultaneously with $(nl)^2/\varepsilon = -4$ fixed to satisfy Ri $= 1 - (nl/2)^2$ along the boundary of the unstable region in Fig. 5a, then γ will keep at the minimum value of $\gamma = -1$. This minimum corresponds to $Y_j/X_j = \infty$. Clearly, when $l \to 0$ and $\varepsilon =$ Ri $- 1 \to 0$ simultaneously, the asymptotic limits of Y_j/X_j and γ will depend on how the ratio $\varepsilon/(nl)^2$ is set. In particular, (B.5) and (B.9) are obtained by setting $(nl)^2/\varepsilon = 0$ and $(nl)^2/\varepsilon = \pm\infty$, respectively. Note that there is a local maximum of $\gamma = 0.76$ at Ri = 1.1 along the left boundary of Fig. 5a. From this local maximum ($\gamma = 0.76$ at Ri = 1.1 and $nl = 0.1$) to the global maximum of $\gamma = 1$ at Ri $= 1_+$ and $nl = 0$, there is a ridge in the region of Ri > 1 (not shown) outside the left boundary of Fig. 5a. There is another local maximum of $\gamma = 0.74$ at Ri = 0.9 along the left boundary of Fig. 5a. From this local maximum ($\gamma = 0.76$ at Ri = 1.1 and $nl = 0.1$) to the global maximum of $\gamma = 1$ at Ri $= 1_-$ and $nl = 0$, there is ridge in the region of Ri < 1 (not shown) outside the left boundary of Fig. 5a. Between the above two ridges, there is a trough of $\gamma = -1$ along the boundary of the unstable region extended to the point of (nl, Ri) = (0, 1_-). This trough becomes infinitely narrow and collapses between the two ridges as $nl \to 0$ outside the left boundary of Fig. 5a. Thus, (nl, Ri) = (0, 1) is a singular point of Y_j/X_j for $j = \pm[2(n - 1) + 1]$ with $m = \pm 1$ (paired slowly propagating modes or paired growing and decaying modes). Depending on how the parameter point (nl, Ri) moves toward this singular point, Y_j/X_j can approach different asymptotic values over the full range from 0 to ∞ and γ can approach different asymptotic value over the full range from -1 to 1.

d. Asymptotic behaviors of X_j/Y_j and γ as Ri $\to \infty$

When $r \equiv f/N$ is fixed, the limit of Ri $\equiv N^2/(\partial_z V)^2 = \varepsilon^{-2} \to \infty$ means that $\partial_z V = \varepsilon N \to 0$ [see (2.3) of Part I]. In this limit, the horizontal length scale defined by $L \equiv H\partial_z V/f$ (see section 2b of in Part I) can be written into $L = \varepsilon H r$. For a fixed wavelength in the dimensional space, this yields $\mu = \varepsilon\mu' \to 0$, where $\mu' = k'/(n\pi) = 2/(nl')$ and l' is the wavelength scaled by $L' \equiv HN/f$ (instead of L), and L' is the Rossby radius of deformation associated with N (instead of $\partial_z V$). Substituting Ri $= \varepsilon^{-2}$ and $\mu = \varepsilon\mu'$ into the roots $\sigma_\pm^2$ of (3.3) of Part I and associated $\beta_\pm$ yields

$$\sigma_+^2 \to -1 + \varepsilon^2(1 + r^2\mu'^2)/|1 - r^2| \quad \text{and}$$
$$\beta_+ \to \varepsilon^{-2}|1 - r^2|/(1 + r^2\mu'^2), \tag{B.10a}$$
$$\sigma_-^2 \to -1 + \mu'^2|1 - r^2|/(1 + r^2\mu'^2) \quad \text{and}$$
$$\beta_+ \to \mu'^{-2}(1 + r^2\mu'^2)/|1 - r^2|. \tag{B.10b}$$

Substituting (B.10a) with Ri $= \varepsilon^{-2}$ and $\mu = \varepsilon\mu'$ into (4.2b)/(4.2a) and (4.6) gives

$$Y_j/X_j \to 1; \quad \gamma \to -1 \quad \text{as} \quad \varepsilon \to 0. \tag{B.11}$$

This result is valid for all j (with $\sigma_j^2 = \sigma_\pm^2$) and is independent of μ'. It is easy to see that (B.11) is consistent with (B.2) in the limit of Ri $\to \infty$ for $\mu = 0$. It is also easy to verify that (B.11) is consistent with (B.4) in the limit of Ri $\to \infty$ for $\mu = \infty$.

Since $\partial_z V \to 0$ in the above limit, all the symmetric modes reduce to the classic inertial gravity wave modes in a nonsheared basic flow. In this case, as indicated by $Y_j/X_j = 1$ in (B.11), the averaged total wave energy is equally partitioned between the cross-band kinetic energy X_j and the along-band kinetic and buoyancy energy Y_j. This result can be also verified directly by using

the equations for the classic inertial gravity waves [such as (8.6.2)–(8.6.4) with (8.4.15) of Gill (1982)]. In the absence of rotation ($f = 0$), the along-band kinetic energy vanishes, so $Y_j/X_j = 1$ in (B.11) recovers the well-known equal partition of the averaged total wave energy between the kinetic energy and buoyancy energy for pure gravity waves (see section 6.7 of Gill 1982). In the presence of rotation, the ratio between the kinetic energy and buoyancy energy is no longer unity and is given by $1 + 2r^2 \tan\varphi'$ where φ' is the vertical tilt angle of the vector wavenumber [see (8.6.6) of Gill (1982)]. In addition to this conventional partition, the result of $Y_j/X_j = 1$ in (B.11) provides another wave energy partition, and this partition retains the neatness of the partition for pure gravity waves as the latter is extended to include the rotational effect. Because $Y_j/X_j = 1$ for $\partial_z V = 0$, the classic inertial gravity wave modes do not produce the nonmodal growths examined in this paper.

APPENDIX C

Solution of (4.3) for Paired Stationary and Linearly Growing Modes

According to (4.9), we have

$$\mathbf{A}_j(0) = X_j \begin{pmatrix} \rho^2 & 0 \\ 0 & 1 \end{pmatrix} \quad \text{and}$$

$$\mathbf{A}_j(\tau) = X_j \begin{pmatrix} \rho^2 & \rho^2\tau \\ \rho^2\tau & 1 + \rho^2\tau^2 \end{pmatrix}, \tag{C.1}$$

where $\rho^2 = Z_j/X_j$. Substituting $\mathbf{A}_j(0)$ and $\mathbf{A}_j(\tau)$ in (C.1) into (4.3) gives $[\mathbf{A}_j(\tau) - \lambda X_j \mathbf{\Lambda}\mathbf{\Lambda}]\mathbf{c}_j = 0$ or, equivalently, $(\mathbf{B}_j - \lambda \mathbf{I})\mathbf{d}_j = 0$, where $\mathbf{\Lambda} = \text{diag}(\rho, 1)$, $\mathbf{d}_j = \Lambda \mathbf{c}_j$ and

$$\mathbf{B}_j = X_j^{-1}\mathbf{\Lambda}^{-1}\mathbf{A}_j(\tau)\mathbf{\Lambda}^{-1} = \begin{pmatrix} 1 & \rho\tau \\ \rho\tau & 1 + \rho^2\tau^2 \end{pmatrix}. \tag{C.2}$$

Substituting (C.2) into $\det(\mathbf{B}_j - \lambda \mathbf{I}) = 0$ gives $\lambda^2 - 2\lambda q_j + 1 = 0$, where

$$q_j = 1 + \rho^2\tau^2/2. \tag{C.3}$$

The two eigenvalues are thus given by

$$\lambda_\pm = q_j \pm (q_j^2 - 1)^{1/2}. \tag{C.4}$$

From (C.3) and (C.4), it is easy to see that $\lambda_\pm = 1$ as $\tau = 0$. As $\tau \to \infty$, $\lambda_+ \to \rho^2\tau^2 \to \infty$ and $\lambda_- \to \rho^{-2}\tau^{-2} \to 0$. In this limit, the eigenvector associated with λ_+ and λ_- are given by $\mathbf{c}_j = (\rho^{-1}\tau^{-1}, 1)^{\mathrm{T}} \to (0, 1)^{\mathrm{T}}$ and $(1, -\rho^{-1}\tau^{-1})^{\mathrm{T}} \to (1, 0)^{\mathrm{T}}$, respectively. Thus, in the limit of $\tau \to \infty$, λ_+ is caused entirely by the linearly growing mode. As shown in (3.8) of Part I for the linearly growing mode, the ψ component is time-invariant and so is the associated cross-band circulation kinetic energy $\{K_2\}$, but the v and b components grow linearly with time and so does their associated energy $\{K_v + P_b\}$. In this case, we have $E(t) = X_j + Z_j t^2$ and $E(\tau)/E(0) = 1 + \tau^2 Z_j/X_j = 1 + \rho^2\tau^2$ for the linearly growing mode. It is easy to verify that $1 < 1 + \rho^2\tau^2 < \lambda_+$ for $0 < \tau < \infty$ and $1 + \rho^2\tau^2 \to \lambda_+$ as $\tau \to \infty$. This means that the energy growth caused by the linearly growing mode approaches the maximum nonmodal growth (in the subspace spanned by the paired stationary and linearly growing modes) as the optimization time approaches infinity.

REFERENCES

Bennetts, D. A., and J. C. Sharp, 1982: The relevance of conditional symmetric instability to the prediction of mesoscale frontal rainbands. *Quart. J. Roy. Meteor. Soc.,* **108,** 595–602.

Buizza, R., and T. N. Palmer, 1995: The singular-vector structure of the atmospheric global circulation. *J. Atmos. Sci.,* **52,** 1434–1456.

Dixon, R. S., K. A. Browning, and G. J. Shutts, 2002: The relation of moist symmetric instability and upper-level potential vorticity anomalies to the observed evolution of cloud heads. *Quart. J. Roy. Meteor. Soc.,* **128,** 839–859.

Farrell, B. F., 1984: Modal and non-modal baroclinic waves. *J. Atmos. Sci.,* **41,** 668–673.

——, and P. J. Ioannou, 1996: Generalized stability theory. I. Autonomous operators. *J. Atmos. Sci.,* **53,** 2025–2040.

Fovell, R., B. Rubin-Oster, and S.-H. Kim, 2004: A discretely propagating nocturnal Oklahoma squall line: Observations and numerical simulations. Preprints, *22th Conf. on Severe Local Storms,* Hyannis, MA, Amer. Meteor. Soc., CD-ROM, 6.1.

Gill, A. E., 1982: *Atmosphere–Ocean Dynamics*. Academic Press, 662 pp.

Koch, S. E., R. E. Golus, and P. B. Dorian, 1988: A mesoscale gravity wave event observed during CCOPE. Part II: Interactions between mesoscale convective systems and the antecedent waves. *Mon. Wea. Rev.,* **116,** 2545–2569.

Parsons, D. B., and H. P. Hobbs, 1983: The mesoscale and microscale structure and organization of clouds and precipitation in midlatitude cyclones. XI: Comparison between observational and theoretical aspects of rainbands. *J. Atmos. Sci.,* **40,** 2377–2397.

Uccellini, L. W., 1975: A case study of apparent gravity wave initiation of severe convective storms. *Mon. Wea. Rev.,* **103,** 497–513.

Xu, Q., 2007: Modal and nonmodal symmetric perturbations. Part I. Completeness of normal modes and constructions of nonmodal solutions. *J. Atmos. Sci.,* **64,** 1745–1763.